Enhanced crystal-field splitting and orbital-selective coherence induced by strong correlations in V_2O_3

Alexander I. Poteryaev,[1] Jan M. Tomczak,[1] Silke Biermann,[1] Antoine Georges,[1] Alexander I. Lichtenstein,[2] Alexey N. Rubtsov,[3] Tanusri Saha-Dasgupta,[4] and Ole K. Andersen[5]

[1]*Centre de Physique Théorique, Ecole Polytechnique, CNRS, 91128 Palaiseau, France*

[2]*I. Institut für Theoretische Physik, Universität Hamburg, Jungiusstraße 9, 20355 Hamburg, Germany*

[3]*Physics Department, Moscow State University, 119992 Moscow, Russia*

[4]*S. N. Bose National Center for Basic Sciences, JD Block, Salt Lake, Kolkata 700 098, India*

[5]*Max-Planck-Institut für Festkörperforschung, Heisenbergstraße 1, D-70569 Stuttgart, Germany*

(Received 7 May 2007; published 27 August 2007)

We present a study of the paramagnetic metallic and insulating phases of vanadium sesquioxide by means of the *N*th order muffin-tin orbital implementation of density functional theory combined with dynamical mean-field theory. The transition is shown to be driven by a correlation-induced enhancement of the crystal-field splitting within the t_{2g} manifold, which results in a suppression of the hybridization between the a_{1g} and e_g^π bands. We discuss the changes in the effective quasiparticle band structure caused by the correlations and the corresponding self-energies. At temperatures of about 400 K, we find the a_{1g} orbital displays coherent quasiparticle behavior, while a large imaginary part of the self-energy and broad features in the spectral function indicate that the e_g^π orbitals are still far above their coherence temperature. The local spectral functions are in excellent agreement with recent bulk sensitive photoemission data. Finally, we also make a prediction for angle-resolved photoemission experiments by calculating momentum-resolved spectral functions.

I. INTRODUCTION

The phase diagram of vanadium sesquioxide has attracted attention of solid-state physicists for decades.[1] Pure, corundum-structured V_2O_3 displays a paramagnetic metallic (PM) phase at ambient pressure and temperature. Cr doping effectively expands the (*ab*) lattice constant and drives the paramagnetic metal into a paramagnetic insulating (PI) phase without changing the crystal symmetry. Application of physical pressure to the Cr-doped compound allows to recover the PM phase, thus leading to a unified phase diagram, in which Cr doping can be considered equivalent to applying negative pressure. The PM and PI phases are separated by a first-order line, which ends in a critical point at about 400 K. Upon cooling below 150 K, long-range antiferromagnetic order sets in, the structure distorts, and the compound becomes insulating [antiferromagnetic insulating (AFI) phase]. Doping with Ti impurities, on the other hand, corresponds to positive pressure. With increasing Ti concentration, the Néel temperature decreases and the AFI phase disappears at about 6% Ti doping.

Doped V_2O_3 thus belongs to the class of materials in which a PM→PI transition can be studied by changing external parameters such as physical or chemical pressure. Numerous experimental studies have led to a detailed picture of the properties: The first-order PM→PI transition is signaled by (i) a spectacular resistivity jump of 2 orders of magnitude,[2,3] (ii) a substantial transfer of spectral weight in the optical conductivity[4] from the low-energy (<0.1 eV) part of the spectrum to higher energies, and (iii) the opening of a gap in the photoemission spectrum.[5–9]

However, already the PM phase is characterized by strong Coulomb-correlation effects: bad metallic behavior of the resistivity, $\rho = 2 \times 10^{-4}$ Ω cm at ambient temperature,[3] strong incoherent features in the optical[4] and photoemission spectra,[8] and a strong mass enhancement as determined from specific heat measurements.[10]

On the theoretical side, different complementary approaches—ranging from electronic structure calculations via theoretical models for the Mott transition to theories combining the two aspects—have been used to access the physics of the rich phase diagram:

McWhan *et al.*[2] emphasized the importance of on-site correlation effects, regarding V_2O_3 as a prototype for a Mott-Hubbard transition. Castellani *et al.*[11] studied a model based on the vanadium t_{2g} Wannier functions split by the trigonal field into a_{1g} and e_g^π orbitals, and they discussed the possibility that in the ground state, one of the V electrons enters a bonding, molecular-orbital state between the a_{1g} orbitals on a vertical V pair, and the other electron enters the doubly degenerate e_g^π level, thus giving rise to a spin $S=1/2$ on each vanadium site. With the advent of dynamical mean-field theory (DMFT), Rozenberg *et al.*[12] investigated the similarities in the phenomenology of the one-band Hubbard model with the phase diagram of V_2O_3. The situation changed when polarization-dependent x-ray absorption measurements of Park *et al.*[13] indicated that the spin is actually $S=1$ in all V_2O_3 phases. This triggered refinements of the theoretical models.[14,15]

Electronic structure calculations by Mattheiss[16] using density-functional theory within the local density approximation (LDA) provided a parameter-free description of the chemical interactions, but they neither captured the insulating nature of the PI phase nor the effects of strong correlations in the PM phase. Nevertheless, by the addition of a few on-site Coulomb-interaction parameters, the LDA forms an accurate starting point for predictive calculations. In particular, the LDA+*U* (unrestricted Hartree-Fock or static mean-

field theory) calculations by Ezhov *et al.*[17] were the first to describe correctly the insulating nature of the low-temperature, antiferromagnetic, monoclinic phase. They found the ground state to have essentially Hund's rule configuration $e_g^{\pi\uparrow\uparrow}$, i.e., the a_{1g} band to be empty. Subsequently, Elfimov *et al.*[18] demonstrated that the shape of the empty $a_{1g}^\uparrow$ band is determined not only by the hopping between the a_{1g} orbitals of a vertical V pair but also by the many horizontal hopping integrals, and Eyert *et al.*[19] showed that the bonding part of the LDA a_{1g} band is strongly hybridized with the e_g^π band. All these observations led to a severe questioning of the $S=1/2$ picture based on the bonding-antibonding splitting of the a_{1g} band, in favor of the $S=1$ picture with two e_g^π electrons and an almost empty a_{1g}. This point of view was forcefully advocated by Sawatzky.[23]

Combined with the LDA, realistic DMFT calculations for V_2O_3 were first performed by Held *et al.*[20,21] As LDA input, they used the local density of states (DOS) projected onto, respectively, the a_{1g} and e_g^π partial waves, truncated outside the vanadium atomic sphere. In this kind of calculation,[22] only the a_{1g} and e_g^π occupations are allowed to adjust through the DMFT iterations toward self-consistency. In an implementation of LDA+DMFT, employing a LDA Hamiltonian, also the orbital characters of each state may adjust, and this, we shall see, is crucial in vanadium sesquioxide where correlations lead to strong changes in the effective hybridizations between the a_{1g} and e_g^π orbital components, an effect which we shall call "correlation-induced dehybridization" in the following. The importance of this effect was emphasized by Sawatzky[23] on the basis of the LDA+U calculations for the AFI phase.[17] Nevertheless, with LDA+DMFT,[20,21] it was possible to obtain high-temperature spectral functions which exhibit lower and upper Hubbard peaks, a gap for the PI phase, and a quasiparticle peak for the PM phase in qualitative agreement with photoemission spectra (PES). However, improvement in the bulk sensitivity of PES for the PM phase at 175 K revealed a quasiparticle peak significantly wider and with more weight than the theoretical one.[8] Using a basis set of t_{2g} Wannier functions, Anisimov *et al.*[24] performed Hamiltonian-based LDA+DMFT calculations and observed some changes from their earlier results.[20,21] However, they did not present a detailed comparison with the improved PES data of Refs. 8 and 9. Laad *et al.*[26] emphasized the role of the crystal-field splitting and studied its influence on the PM-PI transition. Their LDA+DMFT implementation used a density of states approximation and iterative perturbation theory for solving the DMFT equations. In contrast to other LDA+DMFT work, they found the trigonal splitting to be screened out in the PM phase and, as a consequence, the quasiparticle peak to have exclusively a_{1g} character.

In this paper, we use the LDA t_{2g} Wannier functions presented in detail in the preceding paper,[27] referred to as Paper I, in order to construct a Hubbard Hamiltonian, which we solve in the dynamical mean-field approximation. A special effort is made in analytically continuing the quantum Monte Carlo data to the real-frequency axis. This allows, in particular, for a determination of the *correlated* (quasiparticle) band structure of the PM phase. We find excellent agreement with the improved PES data, which encourages us to present and discuss our momentum-resolved spectral function for com-

parison with future angle-resolved PES (ARPES). Our results reveal three key effects of strong correlations which are responsible for the nature of the low-energy behavior. These are (i) a strongly orbital dependent coherence scale, (ii) a considerable enhancement of the effective trigonal splitting between the a_{1g} and e_g^π orbitals, to an extent such that the a_{1g} band is nearly empty, and (iii) a strong reduction of the low-energy bandwidths, associated with a small quasiparticle spectral weight for the a_{1g} orbital. As a result, correlation effects considerably renormalize downward the effective low-energy hybridization between the a_{1g} and e_g^π orbitals. In addition, higher energy structures in the self-energy lead to the expected lower and upper Hubbard bands. These findings provide quantitative support, already for the PM phase, for the $S=1$ picture of two Hund's rule coupled electrons in the e_g^π orbital, as in the AFI phase.[17] We also show that a slight lattice expansion decreases the e_g^π-a_{1g} band overlap, and that because of the strong correlation-induced enhancement of the crystal-field splitting, this leads to the opening of the gap associated with the PI phase.

In Paper I, the details of the corundum structure, the LDA bands, the Wannier functions, and their Hamiltonian generated by the Nth-order muffin-tin orbital (NMTO) method[28] are given. Section II of the present paper briefly reviews the NMTO implementation of LDA+DMFT. Section III presents our results. In Sec. III A, we discuss correlation effects on the low-energy band structure of the paramagnetic phase, showing, in particular, how a correlation-enhanced crystal-field splitting between the a_{1g} and e_g^π bands yields an effective suppression of the hybridization and a nearly empty a_{1g} band. Section III B compares the resulting spectral function to recent photoemission experiments, with excellent agreement. The temperature dependence of both one-particle quantities and local susceptibilities is discussed in Sec. III C. Section III D is devoted to a discussion of the mechanism for the metal-insulator transition, in particular, regarding the role of the correlation-induced enhancement of the crystal-field splitting. Results for the spectral function in the insulating phase are presented in Sec. III F. The appendixes give a detailed summary of both the multiorbital quantum Monte Carlo algorithm by Hirsch and Fye and the continuous time quantum Monte Carlo algorithm by Rubtsov.

II. METHOD

A. Construction of the Wannier Hamiltonian

We construct a realistic many-electron Hamiltonian as the sum of a one-electron part and an on-site Coulomb repulsion, and solve it in the dynamical mean-field approximation. The on-site repulsion depends on the representation (see below), and since we want the Hamiltonian to be both realistic and manageable, we use localized Wannier functions for a low-energy subset of LDA bands, the vanadium t_{2g} bands in the present case. This approach was first described in Ref. 29.

Our LDA Wannier functions are constructed as a symmetrically orthonormalized, minimal set of NMTOs.[28] The three t_{2g} NMTOs for V_2O_3 are shown in Fig. 8 of Paper I (Fig. I.8, in short). Such a basis function has *either* a_{1g}, $e_{g,1}^\pi$, or $e_{g,2}^\pi$ character on the central vanadium site. The NMTOs

on a site transform according to the irreducible representations of the point group, not of the full rotation group like atomic orbitals. For that reason, on-site matrices like the local self-energy and Green's function are diagonal in the NMTO representation. Moreover, an NMTO is maximally localized, in the sense that it has *no* t_{2g} character on any *other* vanadium site. This localization criterion is natural for atom-centered orbitals, but is different from the one used for plane waves which minimizes the spread of the Wannier function.[30] For 3d systems, however, these two different localization criteria yield very similar Wannier functions.[31]

In order for the basis set consisting of the three t_{2g} NMTOs on each vanadium in the solid to span the t_{2g} bands, each basis function must be a solution of Schrödinger's (or Dirac's) differential equation for the single-particle potential, V^{LDA}, for all (in practice $N+1$) energies in the band. This condition fixes all the other partial-wave characters of the t_{2g} NMTOs, that is, *the oxygen and the non-t_{2g} vanadium characters*. The result is seen in Fig. I.8, where, in particular, the oxygen 2p and 3d (e_g^σ) characters on neighboring vanadiums are seen.

The NMTO overlap and Hamiltonan matrices, $\langle \chi_{Rm} | \chi_{R'm'} \rangle$ and $\langle \chi_{Rm} | -\Delta + V^{LDA} | \chi_{R'm'} \rangle$, with R labeling the vanadium sites and m the t_{2g} orbitals, as well as the expansion coefficients of the NMTOs in partial waves, are all given in terms of the Korringa-Kohn-Rostoker Green matrix, downfolded to t_{2g} space and evaluated at the chosen mesh of $N+1$ energies in the t_{2g} band.[28] As may be seen from the bottom panel of Fig. I.5, the t_{2g} bands were reproduced with merely $N=2$. Symmetrical orthonormalization finally yields the NMTO Wannier functions, $\chi_{Rm}^\perp (\mathbf{r} - \mathbf{R})$, and their Hamiltonian matrix,

$$\langle \chi_{Rm}^\perp | -\Delta + V^{LDA} | \chi_{R'm'}^\perp \rangle \equiv H_{Rm,R'm'}^{LDA},$$

whose elements are tabulated in Tables I.I and I.II. Note that $m = (a_{1g}, e_{g,1}^\pi, e_{g,2}^\pi)$ refers to irreducible partner functions of the point group of the vanadium site in question and, hence, to a *local* coordinate system which follows the symmetry operations between the four equivalent vanadium sites in the translational cell.

The complete Hamiltonian of the material is then constructed by supplementing the LDA t_{2g} Hamiltonian with on-site Coulomb interactions:

$$\hat{H} = \hat{H}^{int} + \sum_{Rm,R'm',\sigma} H_{Rm,R'm'}^{LDA} \hat{c}_{Rm}^{\sigma\dagger} \hat{c}_{R'm'}^{\sigma}. \qquad (1)$$

Here, $\hat{c}_{Rm}^{\sigma\dagger}$ ($\hat{c}_{Rm}^{\sigma}$) denotes the creation (annihilation) operator for an electron at site R in orbital m with spin σ, and

$$\hat{H}^{int} =$$

$$\frac{1}{2} \sum_{R,m,m',\sigma} U_{mm'} \hat{n}_{Rm}^{\sigma} \hat{n}_{Rm'}^{-\sigma} + \frac{1}{2} \sum_{R,m\neq m',\sigma} (U_{mm'} - J_{mm'})$$

$$\times \hat{n}_{Rm}^{\sigma} \hat{n}_{Rm'}^{\sigma} \qquad (2)$$

is of Hubbard-Hund type, but can, in principle, contain more general interactions, such as spin-flip and pair-hopping or nonlocal terms. Here, $\hat{n}_{Rm}^{\sigma} = \hat{c}_{Rm}^{\sigma\dagger} \hat{c}_{Rm}^{\sigma}$ is the particle number

operator, and $U_{mm'}$ and $J_{mm'}$ are Coulomb and exchange matrices, which for t_{2g} electrons can be parametrized[32] as follows: $U_{mm} = U$ is the Coulomb repulsion between electrons in the same orbital, $U_{m\neq m'} = U - 2J \equiv U'$ is the average repulsion, and $J_{m\neq m'} = J$ is the Hund's rule coupling. The latter depends only weakly on electronic screening in the solid and, thus, varies relatively little from compound to compound; for transition-metal oxides, values of about 0.7 eV have been estimated[13,33] and this is the value we used. In this work, we restrict ourselves to the form of the interaction given in Eq. (2), which allows us to use the quantum Monte Carlo (QMC) algorithm by Hirsch and Fye.

B. Dynamical mean-field treatment

The resulting Hamiltonian (1) is then treated within dynamical mean-field theory, i.e., the self-energy is approximated by the self-energy of an effective local impurity problem embedded in an energy-dependent bath. This effective system is defined in terms of an effective action

$$S_{eff} = - \int_0^\beta d\tau \int_0^\beta d\tau' \sum_{m,m',\sigma} c_m^{\sigma\dagger}(\tau) [\mathcal{G}^{-1}(\tau - \tau')]_{mm'}^\sigma c_m^\sigma(\tau')$$

$$+ \frac{1}{2} \int_0^\beta d\tau \left\{ \sum_{m,m',\sigma} U_{mm'} n_m^\sigma(\tau) n_{m'}^{-\sigma}(\tau) + \sum_{m\neq m',\sigma} (U_{mm'} - J_{mm'}) n_m^\sigma(\tau) n_{m'}^\sigma(\tau) \right\}, \qquad (3)$$

involving the *bath Green's function* $\mathcal{G}$ which describes the energy, orbital, spin, and temperature dependent interactions of a given correlated atom with the rest of the crystal. $c_m^{\sigma\dagger}(\tau)$ and $c_m^\sigma(\tau)$ are Grassmann variables associated with the creation and annihilation operators introduced above. The bath Green's function has to be determined in a self-consistent way, following the general spirit of a mean-field theory.

The solution of the effective problem implies the calculation of the impurity Green's function

$$G_{mm'}^{loc}(\tau - \tau') = - \langle \mathcal{T} c_m^\sigma(\tau) c_{m'}^{\sigma+}(\tau') \rangle_{S_{eff}}, \qquad (4)$$

where the subscript indicates that the average is to be performed using the effective action (3). This step is the most difficult within dynamical mean-field calculations. Different "impurity solvers" have been designed for this purpose. In the present paper, we use the multiband quantum Monte Carlo schemes by Hirsch-Fye[34] and by Rubtsov,[35] which, in contrast to approximate solver schemes such as iterative perturbation theory[26,36] or schemes based on the noncrossing approximation,[37] have the advantage of yielding numerically exact solutions to the problem. The algorithms are summarized in Appendixes A and B.

In the present case, G^{loc} and the self-energy are diagonal in m because on-site N MTO matrices transform according to the irreducible representations of the point group. Therefore, all local quantities will carry only one orbital index in the following.

Once the impurity Green's function is known, the self-energy of the effective problem can be obtained as

$$\Sigma_m(\omega) = \mathcal{G}_m(\omega)^{-1} - G_m^{loc}(\omega)^{-1} \quad (5)$$

for the imaginary Matsubara frequencies, i.e., for $\omega = i\omega_n = i(2n+1)\pi kT$. The dynamical mean-field approximation now amounts to using the self-energy Σ_m of the effective problem as an approximation to the full nonlocal self-energy of the solid. That is,

$$-G_m^{loc}(\omega) \equiv -G_{mm}^{loc}(\omega) = [H^{LDA} - \mu + \Sigma(\omega) - \omega]_{Rm,Rm}^{-1},$$
$$\quad (6)$$

where the elements of the matrix to be inverted are

$$H_{Rm,R'm'}^{LDA} + [\Sigma_m(\omega) - \omega - \mu)]\delta_{mm'}\delta_{RR'} = -G^{-1}(\omega)_{Rm,R'm'}.$$
$$\quad (7)$$

We obtain the 3×3 on-site Green matrix (6) by first Fourier summing $\Sigma_T \exp(i\mathbf{k} \cdot \mathbf{T})$ the secular matrix (7) over the lattice translations, $\mathbf{T} = \mathbf{R} - \mathbf{R}'$, to the Bloch representation, yielding

$$H_{Im,I'm'}^{LDA}(\mathbf{k}) + [\Sigma_m(\omega) - \omega - \mu]\delta_{mm'}\delta_{II'} = -G^{-1}(\mathbf{k},\omega)_{Im,I'm'},$$
$$\quad (8)$$

in which I and I' label the four vanadium sites in the primitive cell. This 12×12 matrix (8) is then inverted for each $\mathbf{k}$ to give $G(\mathbf{k}, i\omega_n)$. Finally, one of its four on-site blocks is integrated over $\mathbf{k}$ to form the local 3×3 Green matrix (6). Since the latter is diagonal, it suffices to calculate the diagonal a_{1g}, $e_{g,1}^\pi$, and $e_{g,2}^\pi$ elements.

In order to close the set of equations in a self-consistent way, the effective bath propagator is determined from Dyson's equation using the local Green's function of the solid which, according to DMFT, is required to equal the Green's function of the local effective problem. Iteration of this loop yields the dynamical mean-field solution of the Hamiltonian (1).

Finally, a few remarks are as follows:

(i) *Choice of local orbitals and of basis set.* As stressed above, the local Green's function G^{loc} as well as the local self-energy Σ and the local, energy-dependent effective Weiss field $\mathcal{G}^{-1}$ are expressed in the t_{2g} Wannier representation. These quantities are thus (diagonal) 3×3 matrices in orbital space. The necessity of introducing a set of localized orbitals is intimately related to the dynamical mean-field concept: indeed, the notion of locality, which has a natural meaning in the context of *lattice models* of correlated fermions, does not have a basis-independent sense in the solid. However, as soon as a set of localized orbitals has been specified, the distinction between local and nonlocal quantities can, in an obvious way, be replaced by the distinction between on- and off-site ones. The latter notion acquires a well-defined meaning within classical muffin-tin- or atomic-sphere-based methods, but can, in fact, also be realized within different sets of Wannier functions or atomiclike orbitals. We stress that the orbitals in which the impurity model is expressed do not have to coincide with the basis set used for the implementation of the DMFT self-consistency condition. It is for technical convenience that here we use the NMTO basis set for both. For a general discussion of these points, see Ref. 31.

(ii) *Double-counting correction.* In general, a double-counting correction has to be subtracted from the LDA Hamiltonian once Coulomb interactions are treated explicitly. In the present case of an effective Hamiltonian only containing correlated states, an important simplification occurs. As the double-counting term is orbital independent, it amounts to a mere shift of the origin of the energy and can, thus, be absorbed into the chemical potential $\mu = \mu_{true} + \zeta_{dc}$. In practice, it is then sufficient to determine the chemical potential in such a way that the correct particle number is obtained.

$$\hat{H} - \mu_{true}\hat{N} = \hat{H}^{LDA} - \zeta_{dc}\hat{N} - \mu_{true}\hat{N} = \hat{H}^{LDA} - \mu\hat{N}.$$

(iii) *Self-consistent local density.* For the sake of simplicity, we restricted the above description to the one-shot LDA+DMFT approach, in which the LDA Hamiltonian is calculated, once and for all, at the beginning. However, the method is, in principle, not restricted to this case: it is possible to recalculate at the end of the converged DMFT cycle the density of the system, to determine the NMTO-LDA Hamiltonian corresponding to this new density, and to iterate the above procedure for this new Hamiltonian. By iterating until global self-consistency is reached, one obtains an NMTO implementation of the full LDA+DMFT scheme. While in the NMTO context, this has so far not been implemented; analogous calculations have been done in the LMTO and Korringa-Kohn-Rostoker framework.[38]

(iv) *Choice of the U matrix.* As mentioned above, the interaction vertex which supplements the LDA Hamiltonian can be parametrized in terms of two parameters, U and J, corresponding to the intraorbital Coulomb interaction and Hund's rule coupling, respectively. Whereas $J = 0.7$ eV is a generally accepted value for an early transition-metal oxide (hardly changed from its atomic value), the precise determination of U is a delicate issue. The Coulomb interaction depends not only on the choice of representation, but also crucially on the electronic structure of the compound because U is strongly screened. For metallic systems, *ab initio* techniques such as constrained LDA give only rough estimates. As a consequence, we treat U as an adjustable parameter. With the LDA Hamiltonian calculated for the crystal structure of pure V_2O_3 at room temperature in Paper I, we found (see next section) the LDA+DMFT solution to be insulating for $U > U_c \sim 4.35$ eV, i.e., for $U_c' \sim 2.95$ eV, and the best agreement with PM experimental data to be obtained with $U = 4.2$ eV, i.e., with $U' = 2.8$ eV. With the same value of U, we also correctly describe the insulating behavior of Cr-doped V_2O_3.

C. Calculation of real-frequency quantities

ARPES measures $A(\mathbf{k}, \omega) = -\frac{1}{\pi}\text{Tr}\mathfrak{I}G(\mathbf{k}, \omega + i0^+)$, so in order to predict such spectra we need to analytically continue the self-energies $\Sigma_m(i\omega_n)$ from imaginary to real frequencies. We do this by first analytically continuing the local Green's function obtained from a QMC calculation by using the maximum entropy algorithm.[39] The latter yields the local spectral function, $A_m(\omega) = \Sigma_{\mathbf{k}}A_m(\mathbf{k}, \omega)$ from which the local
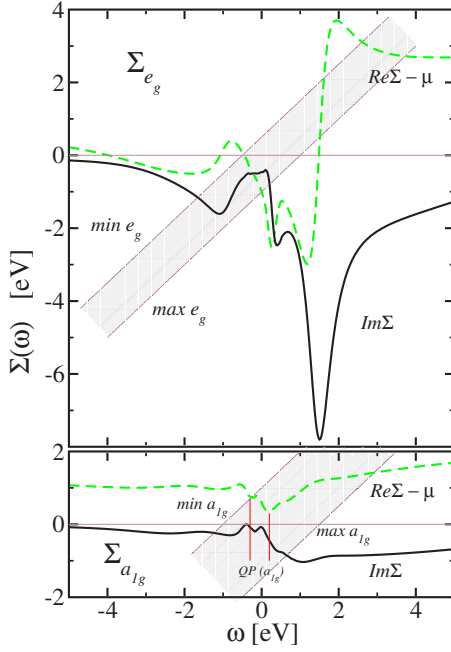
FIG. 1. (Color online) e_g^π and a_{1g} self-energies, $\Sigma_m(\omega)$, as functions of real energy ω, calculated by LDA+DMFT using U =4.2 eV, J=0.7 eV, and T=390 K. Solid (black) and dashed (green) lines are, respectively, the imaginary and real parts of the self-energies. The chemical potential μ=−3.63 eV was subtracted from the real parts. The gray stripes show the extent of the unhybridized LDA bands. Their intersection with the real part of the self-energies roughly indicates solutions of Eq. (9). These solutions give rise to coherent quasiparticles provided the imaginary part of the self-energy is small, which for the a_{1g} orbitals is true within an energy range around the Fermi level indicated by the vertical red lines. For the e_g^π, the large imaginary part indicates that these orbitals stay in an incoherent regime all the way down to 390 K. See text for a discussion.

Green's function on the real-frequency axis is reconstructed by Kramers-Kronig transformation:

$$G_m(\omega + i0^+) = \int d\omega' \frac{A_m(\omega')}{\omega - \omega'} - i\pi A_m(\omega).$$

Finally, we use a root-finding algorithm to solve the coupled equations

$$\sum_{\mathbf{k}} [\omega + \mu - \hat{H}^{LDA}(\mathbf{k}) - \hat{\Sigma}(\omega)]^{-1}_{mm} = G_m(\omega)$$

for the complex quantities $\Sigma_m(\omega)$. Here, $G_m(\omega)$ is the matrix element of the on-site diagonal Green's function in Eq. (8). In order for this procedure to yield reliable solutions, well-converged Monte Carlo data with low statistical noise are needed. Insufficient statistics immediately manifests itself in yielding spiky self-energies. From our data, we were able to obtain perfectly smooth self-energies (see, e.g., Fig. 1), for which we checked that the corresponding **k**-resolved spectral functions sum up to the total spectral function of Fig. 4. As a further test, we verified that we recover the original data on the imaginary-frequency axis from a Hilbert transform of the real-frequency self-energy data. Below we analyze both the

orbital-resolved self-energies and the **k**-resolved spectral functions obtained from them. For more details about the method, see Ref. 40. For previous work on analytical continuations of self-energies, see Refs. 24 and 42–44, and for early techniques to calculate **k**-resolved spectra, see Refs. 45 and 46.

III. RESULTS

A. Correlated paramagnetic metallic phase: Self-energies, quasiparticle band structure, and Hubbard bands

1. A reminder on LDA bands

In order to understand how correlation effects deeply change the low-energy band structure as compared to the LDA, we briefly recall here the essentials of $H^{LDA}(\mathbf{k})$ as obtained in Paper I.

The LDA t_{2g} bands, $E_j(\mathbf{k})$, are shown in the upper, leftmost part of Fig. I.13. They are seen to extend from min $E_{t_{2g}} \approx -1.0$ eV below to max $E_{t_{2g}} \approx 1.5$ eV above the Fermi level and are, thus, substantially broader than the quasiparticle peak in Fig. 4, and substantially smaller than the distance $\sim U$ between the Hubbard bands. The LDA bands exhibit a_{1g}-e_g^π hybridization, as can be seen by the projection onto the a_{1g} and e_g^π Wannier functions in Fig. I.9: Bands with both a_{1g} and e_g^π characters are hybridized, and such bands are, in particular, found at the bottom of the t_{2g} band near the L and F points.[19] A key quantity is the LDA crystal-field splitting, Δ_{LDA}=0.27 eV, listed in Table I.I, which is an order of magnitude smaller than the t_{2g} bandwidth and of the same size as each of the large a_{1g}-e_g^π integrals for hopping to the three nearest neighbors in the xy plane (Table I.II and bottom of Fig. I.11).

In the leftmost bottom part of Fig. I.13, we show the bands, $\epsilon_{mj}(\mathbf{k})$, which result if all hopping integrals between a_{1g} and e_g^π Wannier functions are set to zero, i.e., the *pure* (or "unhybridized") a_{1g} and e_g^π bands which correspond to the limit of the crystal-field splitting being much larger than the hybridization. These bands differ significantly from the LDA bands: the pure e_g^π band, for instance, extends merely from min $\epsilon_{e_g^\pi} \approx -0.5$ eV to max $\epsilon_{e_g^\pi} \approx 1.0$ eV, and the pure a_{1g} band, extending from min $\epsilon_{a_{1g}} \approx -1.0$ eV to max $\epsilon_{a_{1g}} \approx 1.5$ eV, tails off rather than peaks at the bottom of the band. These observations show that the peak at the bottom of the a_{1g} LDA DOS is due to e_g^π hybridization rather than a bonding-antibonding splitting of the a_{1g} levels. We note in passing that these e_g^π and a_{1g} bands, with the latter displaced upward by ~ 2 eV, are similar to the majority e_g^π and a_{1g} bands resulting from a LDA+U calculation for a ferromagnetically ordered approximation to the AFI phase.[17,18]

2. Effects of the imaginary part of the self-energy: Orbital-selective coherence

To see how strong Coulomb interactions alter the low-energy properties of the system, we calculate the self-energy, which encodes all correlations beyond the LDA. We briefly recall what is expected on general grounds from Fermi-liquid theory, before proceeding to a detailed analysis of the orbital-

resolved self-energy $\Sigma_m(\omega)$ as calculated from LDA+DMFT.

In a Fermi liquid, the imaginary part of the self-energy behaves as

$$\Im\Sigma_m(\omega) = -B_m[\omega^2 + (\pi T)^2] + O(\omega^4),$$

thus indicating the existence of infinite-lifetime excitations at zero temperature and on the Fermi surface. However, quasiparticle lifetimes become shorter when moving away from the Fermi surface or at finite temperature, and fade away completely beyond the coherence temperature.

In the low-energy range where the imaginary part of the self-energy is small, the quasiparticle dispersion $\omega_j(\mathbf{k})$ is given by the poles of the $\mathbf{k}$-resolved Green's function:

$$\det[\hat{H}^{LDA}(\mathbf{k}) + \Re\hat{\Sigma}(\omega + i0^+) - \mu - \omega] = 0. \quad (9)$$

In V_2O_3, low-temperature properties are dominated by the onset of antiferromagnetic order. The paramagnetic phase of the pure zero-pressure compound only exists down to about 150 K. For technical reasons related to the high computational cost of QMC calculations at low temperatures, our calculations are done at an even higher temperature. The first issue we have to address in the analysis of the self-energies is, thus, the question of coherence.

Figure 1 displays the real and imaginary parts of both orbital components of the self-energy on the real-frequency axis as obtained from our LDA+DMFT calculation at 390 K. As seen from the lower panel, the imaginary part of the self-energy for the a_{1g} orbitals indeed exhibits a dip at the Fermi level, with a small value of $\Im\Sigma(0)$. The e_g^π orbitals, however, display a zero-frequency value of the imaginary part of the self-energy as large as 0.45 eV, demonstrating that the coherence temperature of the e_g^π orbitals has not yet been reached, i.e., Fermi-liquid theory does not apply.

In Fig. 2, we show the imaginary parts of the self-energies on the imaginary axis, which are a direct output of the QMC. Calculations were performed for $T \sim 390$, 580, and 1160 K ($\beta = 30$, 20, and 10 eV^{-1}) and allow one to study the evolution of the self-energies with temperature. We first note that the zero-frequency value for the lowest temperature coincides with those of the real-axis self-energies displayed in Fig. 1, thus confirming the observation of the a_{1g} orbitals being much closer to their coherent regime than the e_g^π orbitals. The changes with temperature of the self-energy of the scarcely occupied a_{1g} orbital is huge, possibly due to temperature-induced changes in the occupation, which are large on a relative scale. Indeed, the occupation of the a_{1g} orbital evolves from 0.31 via 0.23 to 0.20 electrons per V atom for T decreasing from 1160 K, over 580 K, to 390 K ($\beta = 10$, 20, and 30 eV^{-1}). The radical change between the 1160 and 580 K curves may correspond to reaching the coherent regime for the a_{1g} orbitals. For the e_g^π orbitals, however, the temperature dependence seems to be weaker, and they clearly stay incoherent all the way down to 390 K.

3. Effects of the real parts of the self-energy

We now comment on the shape of the self-energy curves on the real-frequency axis, displayed in Fig. 1 for both or-
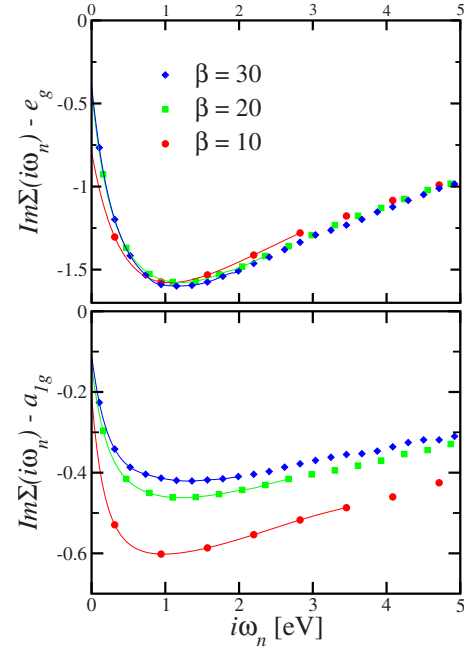

FIG. 2. (Color online) Imaginary parts of the Matsubara frequency self-energies for e_g^π (top) and a_{1g} (bottom) orbitals for different temperatures. (Red) Dots, (green) squares, and (blue) diamonds correspond to $\sim$1160, 580, and 390 K, respectively. Symbols represent raw data, while lines are extrapolations to zero frequency. $U = 4.2$ eV and $J = 0.7$ eV.

bital components, starting from low energy and moving toward higher energy. The first striking observation is that the zero-frequency values of the self-energies lead to a considerable enhancement of the effective crystal-field splitting:

$$\Delta_{\text{eff}} = \Delta_{\text{bare}} + \Re\Sigma_{a_{1g}}(0) - \Re\Sigma_{e_g^\pi}(0). \quad (10)$$

Here, Δ_{bare} is the crystal-field splitting of the unhybridized (pure) LDA bands (see below). While Δ_{bare}, as mentioned above, is 0.27 eV, the self-energy effects yield $\Delta_{\text{eff}} \simeq 1.9$ eV, hence a correlation-induced enhancement by a factor $\sim$7, almost an order of magnitude! The a_{1g} orbital is pushed upward in energy, while the e_g^π orbitals are pushed downward to an extent that two bands hardly overlap anymore. Hence, this is accompanied by a strong enhancement of the orbital polarization in favor of the e_g^π's. Because the occupancy of the a_{1g} orbital is low, the frequency dependence of the self-energy is significantly smaller ($\lesssim 1$ eV) for this orbital. Since the a_{1g} and e_g^π bands hybridize for each $\mathbf{k}$ point, increasing the crystal-field splitting changes the band structure and the constant-energy surfaces in a nontrivial way, which is explained in detail in the following.

When moving away from $\omega = 0$, the imaginary part of the a_{1g} self-energy is small ($\propto \omega^2$) over a narrow range of frequency, from about -0.5 eV below to about 0.1 eV above the chemical potential. In that (Fermi-liquid) range, the real parts of the self-energy roughly obey a linear behavior:[47]

$$\Re\Sigma_m(\omega) = \Sigma_m(0) + (1 - 1/Z_m)\omega + O(\omega^3). \quad (11)$$

The Z's are the quasiparticle spectral weights, corresponding also to the inverse of the effective mass enhancements. We

find $m^*/m = 1/Z_{a_{1g}} \simeq 2.5$, indicating strong correlations; for the e_g^π orbitals, we formally calculate the weights to $1/Z_{e_g}$ $\simeq 5$, even if—as discussed above—these orbitals are far from their Fermi-liquid regime.

Let us finally turn to the high-frequency behavior of the e_g^π self-energy (as mentioned, the a_{1g} has a much weaker frequency dependence). For $2 \text{ eV} < |\omega| < 5 \text{ eV}$, $\mathfrak{R}\Sigma_{e_g}$ behaves approximately as $C_\pm + \Omega_\pm^2/\omega$, where $C_\pm$ and $\Omega_\pm$ control the shape and location of the Hubbard bands (see Fig. 1). For much larger $|\omega|$ (outside the range of the Fig. 1), we checked that

$$\Sigma(\pm\infty)_m = \Sigma_m^{Hartree} = U n_m + (2U - 5J) \sum_{m' \neq m} n_{m'}$$

is equal to the Hartree term (≈ 4.6 and 4.8 eV for the e_g^π and a_{1g} orbitals, respectively). In order to match together the low-frequency and high-frequency behaviors, the e_g^π self-energy must display a very strong frequency dependence at intermediate frequencies, e.g., for $\omega \simeq +1.7 \text{ eV}$ on the positive frequency side. In this region, the self-energy is well approximated by $\Sigma(+\infty) + \frac{\Omega_+^2}{\omega - 1.7 \text{ eV}}$, corresponding to an almost polelike behavior. Correspondingly, the imaginary part displays a pronounced peak at $\omega \simeq 1.7 \text{ eV}$, whose main effect is to strongly deplete the spectral weight in this energy range (see Sec. III A 5 below and Fig. 4).

4. Correlated band structure

As seen above, the imaginary part of the self-energy of the a_{1g} orbitals is tiny in a small energy range around the Fermi level. This motivates us to attempt a description in terms of effective bands, even if, as seen above, one should not think in terms of quasiparticle excitations for the e_g^π orbitals. First, we shall limit ourselves to a simplified but instructive graphical discussion. In the case of degenerate bands, we find the solutions of Eq. (9) for a given energy ϵ as the intersections $\mathfrak{R}\Sigma(\omega) = \omega + \mu - \epsilon$. In other words, the solutions lie where the self-energy crosses a stripe that is linear in frequency and which extends over the LDA bandwidth over which ϵ varies. In the nondegenerate case, a similar construction applies approximately when intersecting the real part of the self-energy with the unhybridized LDA band structure: In Fig. 1, we plot a stripe the width of which corresponds to the width of this unhybridized band structure.[48]

In view of Fig. 1 and the above discussion we expect solutions over a wide range of frequency, extending roughly from −2 to 4 eV. However, only in regions where the imaginary parts of the self-energies are small, these will give rise to coherent quasiparticles, which is true within ±0.5 eV around the Fermi level, at least for the a_{1g} orbital. The intersections in the range 2.5–4 eV correspond to the upper Hubbard band (see Figs. 1 and 4). In the low-energy region where the imaginary part of the self-energy is small and can, thus, be neglected, we linearize the real part according to Eq. (11). The quasiparticle band structure can then be obtained from the eigenvalues of the matrix:
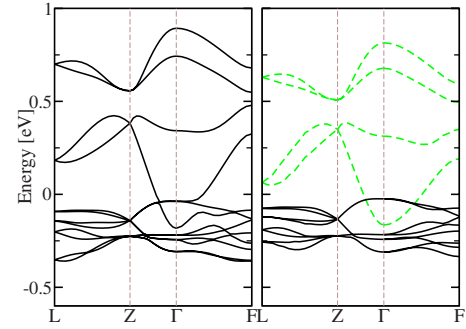

FIG. 3. (Color online) LDA+DMFT quasiparticle bands obtained by truncating the self-energies after linear order in ω. The left-hand panel gives the eigenvalues of the renormalized Hamiltonian (12) and the right-hand side gives the pure e_g^π (black) and a_{1g} (dashed green) band structure, scaled individually according to the scalar expression (13). An a_{1g}-e_g^π hybridization gap is seen between Γ and F points. The self-energy parameters Z_m and $\Sigma_m(0)$ are given in Table I. Note that for the e_g^π orbitals and for the a_{1g} orbitals beyond ~0.5 eV, the linearized bands do not correspond to true quasiparticle states due to a sizable imaginary part of the self-energy (see discussion in the text). Our standard values, U =4.2 eV, J=0.7 eV, and $T \sim 390$ K, were used.

$$Z_m^{1/2}\{H_{Im,I'm'}^{\text{LDA}}(\mathbf{k}) + [\mathfrak{R}\Sigma_m(0) - \mu]\delta_{mm'}\delta_{II'}\}Z_{m'}^{1/2}. \quad (12)$$

The corresponding (linearized) band structure is plotted in the left panel of Fig. 3. The downward shift of the e_g^π bands and the upward shift of the a_{1g}, corresponding to the strong correlation-induced enhancement of the effective crystal field, are clearly visible in this figure. Moreover, we expect that this enhanced crystal field leads to a strong decrease of the hybridization between the a_{1g} and e_g^π bands. Indeed, a simple calculation suggests that the local orbital character of the band is controlled by the parameter $V_\mathbf{k}/\Delta_{\text{eff}}$, with $V_\mathbf{k}$ the bare hybridization (see below). Therefore, we would expect that the hybridization diminishes to a point where the band shapes are close to those of the pure (i.e., unhybridized) bands in the lower, left-hand side of Fig. I.13. The right panel in Fig. 3 demonstrates that this expectation is indeed correct. In this figure, we display the quantities

$$Z_m[\epsilon_{mj}(\mathbf{k}) - \mu + \mathfrak{R}\Sigma_m(0)] \sim \omega_{mj}(\mathbf{k}), \quad (13)$$

that is, the unhybridized LDA bands $\epsilon_{mj}(\mathbf{k})$ each shifted and renormalized according to its linearized $\mathfrak{R}\Sigma_m(\omega)$. The good agreement between the two panels in Fig. 3 demonstrates that the low-energy quasiparticle band structure can be entirely understood as a combination of (i) a considerable enhancement of the effective crystal field and a corresponding unhybridization of the a_{1g} and e_g^π orbitals, and (ii) a (Brinkman-Rice) bandwidth reduction given by the Z_m's, i.e., a mass enhancement of about 2.5 for the a_{1g} and 5 for the e_g^π orbitals. This is entirely consistent with Sawatzky's line of argument.[17,23] As a result, the a_{1g} band *nearly empties* and its bottom tail merely straddles off the top of the e_g^π band, similar to what was found in LDA+U calculations for the AFI structure.[17,18] Correspondingly, the Fermi surface is strongly modified by the correlations.
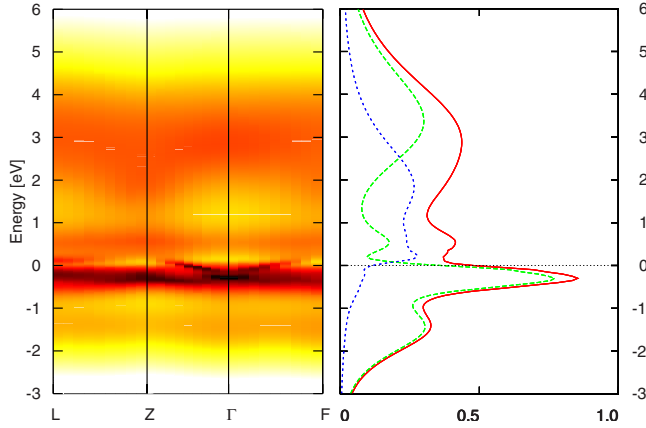
FIG. 4. (Color online) Left-hand side: Intensity plot of the **k**-resolved spectral function $A(\mathbf{k},\omega)$ calculated by LDA+DMFT for U=4.2 eV, J=0.7 eV, and $T\sim$390 K. The total and orbitally resolved spectral functions are shown on the right-hand side. Solid (red) line represents the total spectral function, dashed (green) and dot-dashed (blue) lines are for the e_g^π and a_{1g} orbitals, respectively.

At low energy, the frequency-dependent self-energies $\Sigma_m(\omega)$ shift, shape, and dehybridize the bands in a way that reminds one of the effect of the potential functions in canonical band theory, in particular, for alloys in the coherent potential approximation.[49]

5. Momentum-resolved spectral function

When leaving the low-frequency region in which the self-energies may be linearized, the full complex self-energies must be used and the spectral function $A(\mathbf{k},\omega)$ $=-\frac{1}{\pi}\mathrm{Tr}\,\Im G(\mathbf{k},\omega)$ has to be calculated. The result is given in Fig. 4 for our favorite set of parameters, U=4.2 eV, J=0.7 eV, and $T\sim$390 K. The quasiparticle bands discussed above are clearly visible on this intensity plot and fairly well defined. They lie in the region from -0.5 to 1 eV. Only the top of the a_{1g} band becomes diffuse, and this, only away from the zone center, Γ. The nearly half-filled e_g^π band transfers weight to incoherent Hubbard bands: a weak, narrow, lower band near -1.5 eV and a strong, broad, upper Hubbard band centered at U' and extending from 2 to 4 eV. The depletion of the spectral weight in the $\sim+1.7$ eV range is due to the large imaginary part of the self-energy in this energy range. The lower Hubbard band and the bottom of the upper Hubbard band disperse a bit. On the right-hand side of Fig. 4, we show the a_{1g} and e_g^π momentum-integrated (i.e., on-site) spectral functions. The large, narrow e_g^π peak ($1/Z_{e_g^\pi}$=5) slightly below the Fermi level, and the broader a_{1g} quasiparticle peak ($1/Z_{a_{1g}}$=2.5) above the Fermi level are easily recognized. The remaining e_g^π spectral weight is transferred to higher energies, where Hubbard bands, reminiscent of atomiclike excitations, are developed. Their presence already in the PM state is a characteristic feature of a correlated metal.

Finally, in Fig. 5, we plot the **k**-resolved spectra for the sake of comparison with future angle-resolved photoemission experiments.
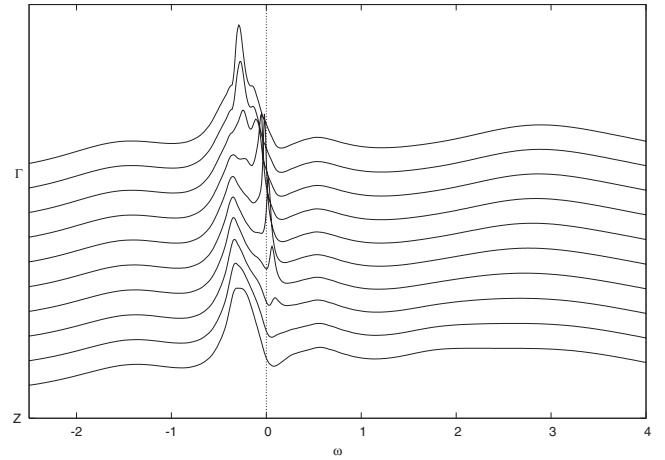

FIG. 5. Momentum-resolved spectra of the PM phase of V_2O_3 along the Γ-Z direction (Ref. 41). Parameters as in Fig. 4.

B. Comparison with photoemission experiments

In Fig. 6, we compare the DMFT spectrum, multiplied with the Fermi function and broadened by an estimated experimental resolution of 90 meV, with the recent, more bulk-sensitive PES data of Mo *et al.*[8] obtained at T=175 K. Although, for reasons of computational cost, our DMFT calculation of the spectral function was performed at 390 K, the agreement is excellent. The positions and relative weights of the quasiparticle peak and the weak, lower Hubbard peak, as well as the approximate form of the former, are correctly captured by the theoretical curve. The fact that the height of the experimental quasi-particle peak is slightly lower than in theory might be due to remaining surface contributions in the experiment, even in the spectra taken at a photon energy of 700 eV. Now that we have unveiled the nature of the quasiparticle peaks and the importance of dehybridization effects due to correlations, the reason why our calculation agrees better with the PES data than the calculations of Keller *et al.*,[21] whose quasiparticle peak was too narrow, is obvious. The Hamiltonian implementations of LDA+DMFT (Refs. 24, 29, 45, 46, and 50) such as the one
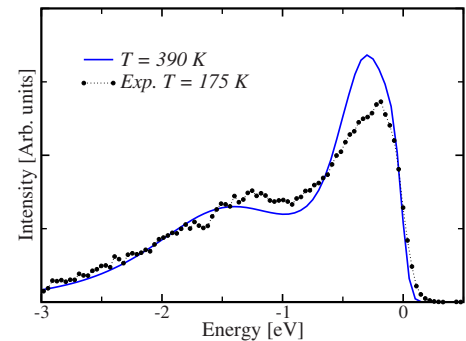

FIG. 6. (Color online) Comparison of the recent experimental PES at T=175 K of Mo *et al.* (Ref. 8) (black dots) with the total spectral function (blue solid) from Fig. 4, convoluted with the Fermi function for T=175 K and broadened with the experimental resolution of 90 meV.
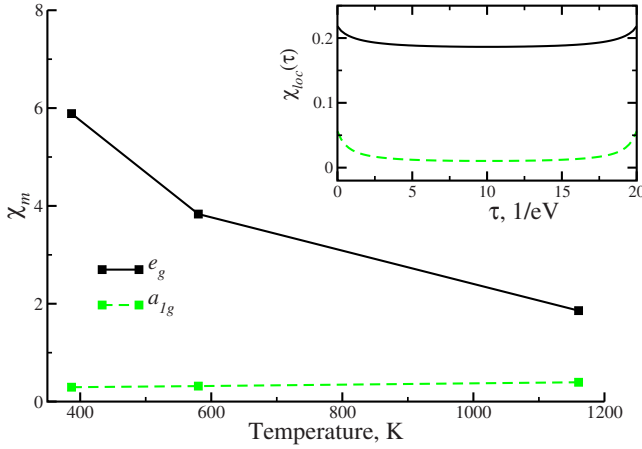
FIG. 7. (Color online) The orbital components of the local magnetic susceptibility χ_m versus temperature for $U=4.2$ and $J=0.7$ eV. Inset: $\chi_{loc}(\tau)$ for 580 K. (Green) Dashed and (black) solid lines correspond to a_{1g} and e_g^π, respectively.

presented in this paper, thus, seem to be important when aiming at a quantitative description of the physics of correlated materials.

C. Temperature dependence, coherence scales, and local moments

The temperature dependent gap filling in the insulating phase has been studied extensively, both experimentally and theoretically, in Ref. 9. Here, we focus on the temperature dependence of one-particle quantities and orbital-resolved local susceptibilities in the high-temperature metallic phase. On general grounds, correlated metals are expected to display a crossover from coherent low-temperature behavior to bad-metal high-temperature properties, at a temperature corresponding to the quasiparticle coherence scale of the material. For V_2O_3, we have found this coherence scale to be

orbital selective and to be of the order of 400 K for the a_{1g} orbitals, but substantially lower for the e_g^π. This order of magnitude is consistent with the sizable mass enhancement[10] (and with the experimentally measured bad conductivity of the metallic phase[3]).

We have also calculated the orbital-resolved local spin susceptibility $\chi_m = \int d\tau \chi_m^{loc}(\tau)$ from the local spin-spin correlation function $\chi_m^{loc}(\tau) = \frac{1}{4}\langle(n_{m\uparrow}(\tau)-n_{m\downarrow}(\tau))(n_{m\uparrow}(0)-n_{m\downarrow}(0))\rangle$. These quantities, plotted as a function of temperature in Fig. 7, display clear local moment behavior (corresponding to an increasing susceptibility upon lowering T) for the e_g^π orbitals, while the a_{1g} susceptibility is flat and small, corresponding to the tiny occupation of these orbitals and their more delocalized bandlike character. For the e_g^π orbitals, we further note that for temperatures between 600 and 400 K, one has not yet reached the regime of saturation where the local moment would be screened. This is in line with the above observation of an incoherent regime of the e_g^π orbitals down to 390 K.

D. Crystal-field enhancement for increasing U

We have seen above that one of the key effects of strong correlations for this material is to considerably enhance the effective crystal-field splitting between the e_g^π and a_{1g} orbitals, and to correspondingly increase the orbital polarization in favor of the e_g^π. In this section, we briefly discuss how these effects evolve as the value of the parameter U is increased.

The quasiparticle weights, the Wannier-orbital populations and the renormalized crystal field are given in Table I for several values of U. These low-frequency quantities were extracted directly from the imaginary frequency QMC self-energies displayed in Fig. 8 [the Z_m's are obtained by extrapolating the low-frequency behavior of the self-energy to zero frequency and analyzing the slope of the linear regime of $\Im\Sigma_m(i\omega_n)$]. As discussed above, the a_{1g} self-energy has a weaker frequency dependence because of its lower occu-

TABLE I. Effective crystal-field splitting [Eq. (10)], extrapolated to zero, real parts of the self-energy, quasiparticle parameters, and Wannier-function occupations for increasing values of U ($J=0.7$ eV is fixed). Note that the Z factors for the e_g^π orbitals are purely formal quantities, see text for a discussion. The values at $U=0$ eV are the LDA ones. The LDA t_{2g} bandwidth is 2.5 eV, while those of the pure e_g^π and a_{1g} LDA bands are, respectively, 1.5 and 2.5 eV. The last column with $U=4.2$ eV and smaller temperature $T \sim 390$ K corresponds to the figures discussed in Secs. III A and III B. Note that $U=4.2$ eV is our favorite choice for the PM phase.

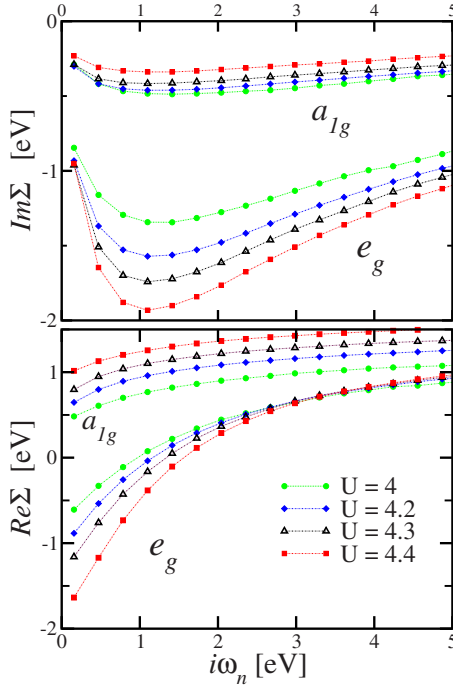| U (eV)		0	4.0	4.2	4.3	4.4	4.2
T (K)		0	580	580	580	580	390
$\Re\Sigma_m(0^+)-\mu$	e_g^π	0	−0.76	−1.00	−1.39	−1.91	−1.01
(eV)	a_{1g}	0	0.42	0.56	0.69	0.93	0.59
Δ_{eff} (eV)		0.27	1.45	1.83	2.35	3.11	1.87
$1/Z_m$	e_g^π	1	3.33	5	5	*ins.*	5
	a_{1g}	1	2	2.5	2.5	*ins.*	2.5
n_m	e_g^π	1.48	1.70	1.78	1.82	1.88	1.80
	a_{1g}	0.52	0.30	0.22	0.18	0.12	0.20

FIG. 8. (Color online) Imaginary and real parts of the self-energies, $\Sigma_m(i\omega_n)$, for the e_g^π and a_{1g} orbitals as functions of imaginary Matsubara frequency and for different values of the Coulomb interaction U. (Green) Dots, (blue) diamonds, (open black) triangles, and (red) squares correspond to $U=4$, 4.2, 4.3, and 4.4 eV, respectively. For $U=4.4$ eV, we find an insulating solution. $J=0.7$ eV and $T=580$ K.

pancy, indicating smaller correlation effects. For both Wannier orbitals, the low-frequency spectral weight Z_m decreases with increasing Coulomb interaction as expected. At the same time, $\Im\Sigma_{a_{1g}}(i\omega_n)$ becomes less frequency dependent with increasing U, while for the strongly correlated e_g^π orbital, the behavior of $\Im\Sigma_{e_g}(i\omega_n)$ is the opposite: it becomes more correlated with increasing U, corresponding to an increasing population of this orbital.

As seen from Table I, the low-frequency effective crystal field increases dramatically as U is increased. The LDA bands in the left-hand side of Fig. I.13 yield a distance of max $\epsilon_{e_g^\pi}-$ min $\epsilon_{a_{1g}}=2.02$ eV from the top of the e_g^π band to the bottom of the a_{1g} band. Since both band extrema are at the Γ point, where a_{1g} and e_g symmetries cannot mix (see Fig. I.9), the hybridized and the pure LDA bands yield the same value. The value 2.02 eV is roughly the self-energy shift needed to push the top of the e_g^π band below and the bottom of the a_{1g} band above the Fermi level and, hence, to cause a metal-insulator transition while keeping the structure of pure V_2O_3 at normal pressure.

From Table I, we realize that the critical value $\Delta_{\text{eff},c}=2.02+0.27=2.29$ eV is reached for $U_c=4.3$ eV. When this value of the Coulomb repulsion is exceeded, the system becomes an insulator with a direct gap (at Γ) between a valence band of e_g^π and a conduction band of a_{1g} character.[51] Albeit driven by on-site Coulomb interactions, this transition is not caused by a divergence of the self-energy at low frequency (like in the Mott transition of the single band model at

particle-hole symmetry), but rather by the fact that effective crystal-field splitting [or $\Sigma_{a_{1g}}(0)-\Sigma_{e_g^\pi}(0)$] is so large that the e_g^π and a_{1g} bands no longer overlap. The population of the e_g^π Wannier function monotonously increases toward 2, and that of the a_{1g} Wannier function decreases toward 0. This is fairly similar to what was recently found for the pressure-induced insulator-metal transition in $LaMnO_3$.[52]

We emphasize that this study as a function of U was performed by keeping the crystal structure of pure V_2O_3 at normal pressure. However, it is clear from this study that a slight decrease of the distance from the top of the e_g^π to the bottom of the a_{1g} LDA band suffices to drive the system from the metallic to the insulating phase. Indeed, the LDA bands for the expanded structure of 3.8% Cr-doped V_2O_3 given on the right-hand side of Fig. I.13 yield max $\epsilon_{e_g^\pi}-$ min $\epsilon_{a_{1g}}$ =1.69 eV, that is, a 0.33 eV decrease from 2.02 eV. This large value is consistent with the fact that the observed conductivity gap[3] in the PI phase always exceeds 0.3 eV. Of this 0.33 eV reduction caused by the Cr-induced expansion of the lattice, 0.17 eV is due to the bottom of the a_{1g} band moving up with respect to the a_{1g} on-site energy, 0.13 eV is due to the top of the e_g^π band moving down, and only 0.03 eV is due to the increase of the crystal-field splitting. Further details are given in Paper I.

With this, we believe to have demystified the nature of the metal-insulator transition in V_2O_3.

E. Hamiltonian dynamical mean-field theory versus fixed hybridization approximation

At this point, a word of comparison between the LDA +DMFT calculations performed in the Hamiltonian form (as in the present paper) and the ones using a density of states integration as an approximation is in order. In practice, it often looks as if the error induced by doing the hybridization approximation [i.e., using a simple Hilbert transform of the density of states instead of the full **k** sum in the self-consistency condition (8)] could be partially compensated by a slightly bigger choice of the Coulomb interaction parameter U, see, e.g., Ref. 53 in comparison with Ref. 29 or the discussion in Ref. 24. In the present case of strong orbital and occupation shifts induced by the correlations, however, the effect of the hybridization approximation is particularly severe: as discussed above, one of the key effects of the correlations in V_2O_3 is the suppression of hybridization of the a_{1g} and e_g^π bands by the correlation-enhanced crystal-field splitting. The fixed hybridization approximation, however, neglects any correlation-driven changes of the hybridization and, thus, entirely overlooks this effect.

This can be rationalized in a simple two-band model. We assume that the symmetries are such that the local Green's function, $G(\omega)=\Sigma_{\mathbf{k}}G(\mathbf{k},\omega)$, is purely diagonal. The momentum-resolved Green's function within DMFT reads

$$G(\mathbf{k},\omega)=\left[\omega+\mu-\begin{pmatrix}\epsilon_{\mathbf{k}}^1 & V_{\mathbf{k}}^*\\V_{\mathbf{k}} & \epsilon_{\mathbf{k}}^2\end{pmatrix}-\begin{pmatrix}\Sigma_1 & 0\\0 & \Sigma_2\end{pmatrix}\right]^{-1}$$

$$=\frac{1}{(\omega+\mu-\epsilon_{\mathbf{k}}^1-\Sigma_1)(\omega+\mu-\epsilon_{\mathbf{k}}^2-\Sigma_2)-|V_{\mathbf{k}}|^2}$$

$$\times\begin{pmatrix}\omega+\mu-\epsilon_{\mathbf{k}}^2-\Sigma_2 & V_{\mathbf{k}}\\V_{\mathbf{k}}^* & \omega+\mu-\epsilon_{\mathbf{k}}^1-\Sigma_1\end{pmatrix}. \quad (14)$$

Both the diagonal and off-diagonal (hybridization-induced) components of the Green's function are, thus, renormalized by the denominator containing the self-energy, and the corresponding eigenvectors adjust at each cycle of the DMFT self-consistently. The fixed hybridization approximation consists instead in replacing the Hamiltonian matrix by its diagonalized version while keeping the self-energy in the form above.

$$G(\mathbf{k},\omega) = \left[\omega + \mu - \begin{pmatrix} E_{\mathbf{k}}^{(+)} & 0 \\ 0 & E_{\mathbf{k}}^{(-)} \end{pmatrix} - \begin{pmatrix} \Sigma_+ & 0 \\ 0 & \Sigma_- \end{pmatrix} \right]^{-1},$$

where

$$E_{\mathbf{k}}^{\pm} = \frac{1}{2}(\epsilon_{\mathbf{k}}^1 + \epsilon_{\mathbf{k}}^2) \pm \frac{1}{2}\sqrt{(\epsilon_{\mathbf{k}}^1 - \epsilon_{\mathbf{k}}^2)^2 + 4|V_{\mathbf{k}}|^2}$$

denote the eigenvalues of the LDA Hamiltonian. Technically, this form is easier to handle because $\mathbf{k}$ sums can be taken by simply integrating over the LDA partial densities of states. There is, however, no way of updating the orbital character that, in general, will be modified under the influence of the correlations. In fact, assuming two bands split by a crystal-field splitting Δ but otherwise degenerate (i.e., $\epsilon_{\mathbf{k}}^1 = \epsilon_{\mathbf{k}}^2 + \Delta$), the eigenvectors of the full matrix problem (14) depend on the self-energy via the renormalized crystal-field splitting $\Delta_{eff} = \Delta + \Sigma_1(0) - \Sigma_2(0)$. The eigenvectors read

$$\sin(\theta_{1/2})|1\rangle + \cos(\theta_{1/2})|2\rangle,$$

with

$$\tan(\theta_{1/2}) = \frac{\Delta_{eff}}{2V_{\mathbf{k}}} \pm \sqrt{\left(\frac{\Delta_{eff}}{2V_{\mathbf{k}}}\right)^2 + 1}.$$

The orbital character, thus, depends on the ratio of the *renormalized* crystal-field splitting over the hybridization, as announced above. In the fixed hybridization approximation, however, the renormalized crystal-field splitting Δ_{eff} in the above decomposition of the eigenvectors onto the basis of the noninteracting nonhybridized single-particle states $|1\rangle$, $|2\rangle$ is replaced by the bare crystal-field splitting Δ. Thus, the orbital characters are fixed once and for all by the LDA Hamiltonian and cannot respond to the correlations.

This approximation is particularly severe in the present case, since the strong enhancement of the crystal-field splitting profoundly modifies the effective hybridization.

F. Paramagnetic insulating phase

We have performed a LDA+DMFT calculation using the expanded crystal structure of the 3.8% Cr-doped material using the same value $U=4.2$ eV as the one used in our study of pure V_2O_3. We note, however, that because the screening in the PI phase is expected to be somewhat less efficient than in the PM phase, it might have been appropriate to also consider a value of U slightly larger. We, nevertheless, keep the same value for the sake of comparison.

The momentum-integrated, orbitally resolved, spectral functions resulting from this calculation (after a MAXENT treatment of the data) are displayed in Fig. 9. It is seen that,
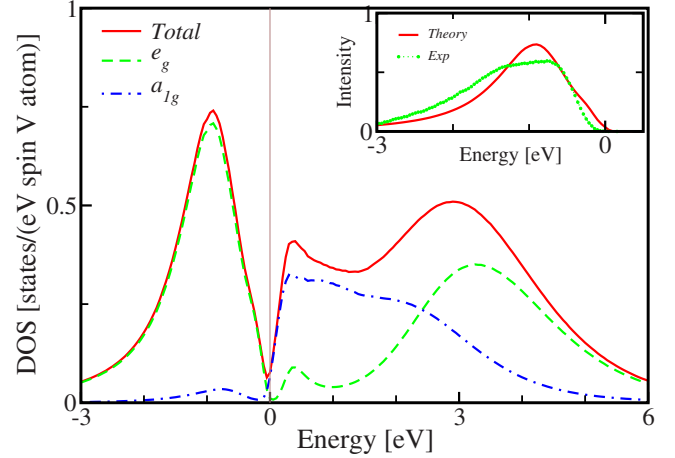

FIG. 9. (Color online) Spectral function for insulating $(V_{0.962}Cr_{0.038})_2O_3$ at $T=580$ K ($\beta=20$ eV^{-1}) calculated by DMFT using the LDA t_{2g} Wannier functions specified in Tables I and II of Paper I. Solid (red) line represents total spectral function, dashed (green) and dot-dashed (blue) lines represent e_g^π and a_{1g} orbitals, respectively. The inset shows a comparison of recent experimental PES at $T=175$ K of Mo *et al.* (Ref. 9) (green dots) with the total spectral function, convoluted with the Fermi function for $T=175$ K and broadened with the experimental resolution of 90 meV. $U=4.2$ eV and $J=0.7$ eV. The chemical potential is at zero energy.

indeed, the quasiparticle features at the Fermi level are almost entirely suppressed. Close examination of the figure (and of the quasiparticle bands—not shown) reveal that the low-frequency spectral weight is small but finite.

Finally, we comment on a technical aspect of this calculation of the PI phase. Because of the almost complete orbital polarization, it proved to be essential to allow for global updates in the QMC calculation. In contrast to the calculations in the PM phase which used the Hirsch-Fye algorithm, we have employed the continuous-time Rubtsov algorithm[35] in the PI phase, with global updates, in order to overcome the tendency of the Hartree-Fock algorithm with local updates to get trapped in a given fully polarized configuration.

G. Comparison with polarization-dependent x-ray absorption

From polarization-dependent x-ray-absorption (XAS) measurements analyzed by means of cluster calculations, Park *et al.*[13] concluded that the PI phase is a 3:2 mixture of the two-electron configurations (e_g^π, e_g^π) and (e_g^π, a_{1g}), and that the PM phase is a 1:1 mixture. This means that in the V 3p core region, the ratio of e_g^π to a_{1g} electrons should be 4:1 in the PI phase and 3:1 in the PM phase. This ratio is between V 3d electrons whose wave functions have different angular, but identical radial behaviors, e.g., the ratio between *partial-wave* e_g^π and a_{1g} *occupations* as defined in Paper I, where Fig. I.9 showed such partial-wave characters for the LDA O 2p and V 3d bands in the PM phase.

Now, for the O 2p band, we do use the LDA and find—by integrating the respective fatness in Fig. I.9 up to the pd gap—that there are 0.32 local e_g^π electrons and 0.18 local a_{1g}

electrons on each vanadium. The PI and PM structures give the same numbers and this is consistent with the fact that the V-O distances are essentially the same.

For the V t_{2g} bands, we use the LDA+DMFT. Since those results are expressed in terms of the $e_{g,1}^\pi$, $e_{g,2}^\pi$, and a_{1g} NMTO Wannier functions shown in Fig. I.8, we need their partial-wave characters, employing the same definitions (atomic-sphere normalization) as in Fig. I.9. When doing so, we find that the a_{1g} NMTO Wannier function has 68% a_{1g} and 6% e_g^π partial-wave character (sum of $e_{g,1}^\pi$ and $e_{g,2}^\pi$), and that each of the e_g^π NMTO Wannier functions has 77% e_g^π and 7% a_{1g} partial-wave character. The presence of $e_g^\pi (a_{1g})$ character in the $a_{1g}(e_g^\pi)$ NMTO Wannier function is caused by N-ization and orthonormalization, as was explained in connection with Fig. I.6.

Our DMFT calculation for the PI phase shows that of the two electrons in the full e_g^π band, 0.10 have a_{1g} Wannier-function character. This number is the integral over the occupied part of the blue, dot-dashed a_{1g} DOS in Fig. 9, and it is caused by the hybridization between the a_{1g} Wannier function and the two e_g^π Wannier functions. In Paper I, this number was estimated roughly, using second-order perturbation theory, as the real-space sum $\Sigma t^2 / \Delta_{eff}$, where t are the a_{1g}-to-e_g^π hopping integrals and $\Delta_{eff} = 1.87$ eV. We took Δ_{eff} to be the same for the PI and PM phases because, as explained above, Δ_{eff} only increases by 0.03 eV when going from the PM to PI phase. This estimate, which neglected the effects of temperature and correlation-induced incoherence, also gave $0.10a_{1g}$ Wannier electrons. We, therefore, believe that this number is fairly robust and not overestimated in the DMFT calculation.

The number of a_{1g} partial-wave electrons in the PI phase is thus

$$0.18 + 0.68 \times 0.10 + 0.07 \times 1.90 = 0.38,$$

and the number of local e_g^π partial-wave electrons is

$$0.32 + 0.77 \times 1.90 + 0.06 \times 0.10 = 1.79,$$

together yielding the ratio $1.79:0.38=4.7$, a bit larger than the XAS result: 4.

For the PM phase, our DMFT calculation (Table I and Fig. 4) gave $0.00a_{1g}$ Wannier electrons. The increase by $0.12a_{1g}$ electrons when going from the PI to the PM phase is essentially the occupation of the metallic a_{1g} electron pocket. The number of local a_{1g} electrons in the PM phase is thus

$$0.18 + 0.68 \times 0.22 + 0.07 \times 1.78 = 0.45,$$

and the number of local e_g^π electrons is

$$0.32 + 0.77 \times 1.78 + 0.06 \times 0.22 = 1.70,$$

together yielding the ratio $1.70:0.45=3.8$, again a bit larger than the XAS result: 3.

IV. CONCLUSION

Summarizing, we have presented a detailed study of the paramagnetic metallic and insulating phases of V_2O_3 within an NMTO-t_{2g}-Hamiltonian implementation of LDA+DMFT.

We have discussed the strong correlation-induced changes in the low-energy quasiparticle band structure of the metallic phase. A correlation-induced enhancement of the crystal-field splitting leads to an unhybridization of the a_{1g} and e_g^π bands and a nearly empty a_{1g} band. The resulting spectral functions are in excellent agreement with recent photoemission experiments. From a technical point of view, the drastic modifications that correlation effects cause in the hybridization of the orbitals explain why LDA+DMFT calculations that neglect these changes compare less favorably to photoemission experiments than Hamiltonian calculations.[20,21,24] We have calculated local and momentum-resolved spectral functions, self-energies, quasiparticle weights, and local spin susceptibilities, and find PM V_2O_3 to be a rather strongly correlated metal with Z of the order of 0.2 and a coherence temperature below 400 K. Interestingly, the material develops strongly orbital-selective coherence scales, with the e_g^π orbitals exhibiting quasiparticle lifetimes shorter than $1/(0.5$ eV) on the Fermi level down to 390 K. Still, our picture is different from that of Laad *et al.*,[26] who described the paramagnetic phase as an orbital-selective Mott phase with a gap (or, due to finite temperature, pseudogap) in the e_g^π orbitals.

We have discussed the transition from the paramagnetic metallic to the paramagnetic insulating phase, the origin of which we tracked down to the correlation-induced enhancement of the crystal-field splitting. Finally, we have calculated the spectral function in the insulating phase, in good agreement with photoemission data. A technical advance employed for this latter calculation was the use of the continuous-time quantum Monte Carlo algorithm,[35] which to our knowledge has not been applied to LDA+DMFT calculations before.

APPENDIX A: MULTIORBITAL HIRSCH-FYE ALGORITHM

As discussed above, solving the DMFT equation requires—at each iteration—the solution of an effective local problem, that is, the calculation of the Green's function (4) with the effective action (3). By using the fermionic path integral formalism, the problem can be stated as follows: for a given Weiss field, one needs to calculate the Green's function

$$G^{\sigma}_{mm'}(\tau - \tau') = -\frac{1}{Z}\mathcal{T}\int D[c^+_{m\sigma}, c_{m'\sigma}]e^{-S_{eff}}c_{m\sigma}(\tau)c^+_{m'\sigma}(\tau'),$$

$$\text{(A1)}$$

where $\mathcal{T}$ denotes the time-ordering operator and Z the partition function

$$Z = \int D[c^+_{m\sigma}, c_{m'\sigma}]e^{-S_{eff}}.$$

$$\text{(A2)}$$

For the solution of this problem, the auxiliary fields QMC method by Hirsch and Fye is used.[34] Here, we review this approach in the multiorbital case.

The imaginary time is discretized in L slices $\tau_i, i = 1, 2, \ldots, L$ of size $\Delta\tau = \beta/L$. Performing a standard Trotter decomposition, one obtains for the partition function:

$$Z = \text{Tr}\prod_{l=1}^{L} e^{-\Delta\tau(H^{LDA}+H^{int})} \simeq \text{Tr}\prod_{l=1}^{L} e^{-\Delta\tau H^{LDA}}e^{-\Delta\tau H^{int}}. \quad \text{(A3)}$$

The quadratic interaction term in the effective action (3) can be decoupled by discrete Hubbard-Stratonovich transformation introduced by Hirsch[54]

$$e^{-\Delta\tau U_{mm'}[n_m n_{m'}-(n_m+n_{m'})/2]} = \frac{1}{2}\sum_{S_{mm'}=\pm1} e^{\lambda_{mm'}S_{mm'}(n_m-n_{m'})},$$

$$\text{(A4)}$$

where $S_{mm'}(\tau)$ are auxiliary Ising fields. Starting from here and in the following, m is a spin-orbital index and U matrix is a general spin and orbital dependent interaction matrix. One field has to be introduced for each pair of spin orbitals and time slice. The coupling of the auxiliary spins to the physical occupations is related to the original Coulomb interaction via

$$\lambda_{mm'} = \text{arccosh}[e^{(1/2)\Delta\tau U_{mm'}}]. \quad \text{(A5)}$$

Using the Hirsch transformation, one can integrate out the fermionic fields in the path integral. The resulting Green's and partition function matrices have the following form:

$$\hat{G}^{\sigma} = \frac{1}{Z}\frac{1}{2^{N_f L}}\sum_{\{S_{mm'}(\tau)\}=\pm1} \hat{G}^{\sigma}(S_{mm'})W(S_{mm'}), \quad \text{(A6)}$$

$$Z = \frac{1}{2^{N_f L}}\sum_{\{S_{mm'}(\tau)\}=\pm1} W(S_{mm'}(\tau)), \quad \text{(A7)}$$

with

$$W(S_{mm'}) \equiv \det[\hat{G}^{-1}_{\uparrow}(S_{mm'})]\det[\hat{G}^{-1}_{\downarrow}(S_{mm'})], \quad \text{(A8)}$$

where $N_f = M(2M-1)$ is the number of Ising fields for the M interacting orbitals and $\hat{G}(S_{mm'})$ is the Green's function for a given configuration of the auxiliary Ising fields:

$$G^{-1}_{mm'}(\tau, \tau'; S) = \mathcal{G}^{-1}_{mm'}(\tau, \tau') + \Delta_m(\tau)\delta_{mm'}\delta_{\tau\tau'},$$

$$\Delta_m(\tau) = e^{V_m(\tau)} - 1,$$

$$V_m(\tau) = \sum_{m'} \lambda_{mm'}S_{mm'}(\tau)\sigma_{mm'}. \quad \text{(A9)}$$

Here, we have introduced the generalized Pauli matrix:

$$\sigma_{mm'} = \begin{cases} +1, & m < m' \\ 0, & m = m' \\ -1, & m > m'. \end{cases} \quad \text{(A10)}$$

In the multiband case at low filling, a numerical problem with $\mathcal{G}$ related to the large absolute value of the chemical potential can occur. In this case, a large part of the $\mathcal{G}(\tau)$ function can be very close to zero, which can be the source of an inversion problem in Eq. (A9). In order to avoid this problem, a technical trick can be introduced: the bath Green's function and effective Hirsch potential are replaced by $\mathcal{G}^{-1} \rightarrow \mathcal{G}^{-1} - \varsigma$ and $V_m(\tau) \rightarrow V_m(\tau) + \varsigma\Delta\tau$. This replacement stems from a specific choice of dividing the noninteracting from the interacting parts of the Hamiltonian. It is exact for all values of the shift ς, which can, thus, be chosen for numerical convenience.

In order to calculate the Green's function, we need, in principle, to integrate over all possible Ising spin configurations $\{S_{mm'}(\tau)\}$. It is this sum that is performed by a Monte Carlo sampling procedure. The Green's functions of two arbitrary configuration are related to each other by the following Dyson equation:

$$G' = [1 + (1 - G)(e^{V'-V} - 1)]^{-1}G. \quad \text{(A11)}$$

Calculating G' from G via this equation reduces the number of operations from the $(ML)^3$ operations necessary for a standard matrix inversion to $(ML)^2$.

Using QMC importance sampling, we integrate over the Ising fields with the absolute value of $W(S_{mm'})$ as a stochastic weight. The Metropolis algorithm is used to perform QMC spin flips in the space of the Ising fields. For a single spin flip $S_{mm'}$, the determinant ratio is calculated as follows:

$$\det[\hat{G}]/\det[\hat{G}'] = R_m R_{m'} - R_{mm'}, \quad \text{(A12)}$$

with

$$R_m = 1 + [1 - G_{mm}(\tau, \tau)]\Delta_m(\tau),$$

$$R_{m'} = 1 + [1 - G_{m'm'}(\tau, \tau)]\Delta_{m'}(\tau),$$

$$R_{mm'} = G_{mm'}(\tau, \tau)\Delta_{m'}(\tau)G_{m'm}(\tau, \tau)\Delta_m(\tau),$$

and the Green's function matrix is updated in the standard two-step update:

$$G'_{m_1 m_2}(\tau_1, \tau_2) = G_{m_1 m_2}(\tau_1, \tau_2) + [G_{m_1 m}(\tau_1, \tau) - \delta_{m_1 m}\delta_{\tau_1, \tau}]$$

$$\times \frac{\Delta_m(\tau)}{R_m(\tau)}G_{mm_2}(\tau, \tau_2), \quad \text{(A13)}$$

$$G^{new}_{m_1 m_2}(\tau_1, \tau_2) = G'_{m_1 m_2}(\tau_1, \tau_2) + [G'_{m_1 m'}(\tau_1, \tau) - \delta_{m_1 m'}\delta_{\tau_1, \tau}]$$

$$\times \frac{\Delta_{m'}(\tau)}{R_{m'}}(\tau)G'_{m'm_2}(\tau, \tau_2). \quad \text{(A14)}$$

The above described QMC algorithm allows one to calculate the Green's function in the general matrix form. This has several advantages: (i) it can be applied to a system with low crystal symmetry, where the effective Weiss field and Green's function matrices cannot be presented in diagonal form; and (ii) one can easily think about m as site-spin-orbital index, and thus without changing any single line in the QMC part of the program, it can be used for cluster DMFT calculations for systems where, e.g., pairs of atoms play an important role.[55,56]

APPENDIX B: CONTINUOUS-TIME QUANTUM MONTE CARLO

The continuous-time fermionic quantum Monte Carlo technique differs from the Hirsch-Fye algorithm in several important aspects. It does not require time discretization and does not use any auxiliary fields. Consequently, the computational complexity is different. A particular advantage over the Hirsch-Fye method can be achieved for an interaction which is nonlocal in space, orbital, and spin indices, or in time. In this appendix, we describe the general ideas of the method and the usage of so-called global updates, which are ways to get rid of local trappings of the continuous-time (CT)-QMC random walker.

We start from the partition function $Z = \mathrm{Tr}\, \mathcal{T} e^{-S}$ for a system with pair interaction in the most general case and split the action S into two parts: an unperturbed action S_0 of Gaussian form and an interaction part W.

$$S = S_0 + W,$$

$$S_0 = \int \int t_r^{r'} c_{r'}^\dagger c^r dr dr',$$

$$W = \int \int \int \int w_{r_1 r_2}^{r_1' r_2'} c_{r_1'}^\dagger c^{r_1} c_{r_2'}^\dagger c^{r_2} dr_1 dr_1' dr_2 dr_2'. \quad \text{(B1)}$$

Here, $\mathcal{T}$ is the time-ordering operator, $r = \{\tau, s, i\}$ is a combination of the continuous imaginary-time variable τ, spin projection s, and the discrete index i numbering the single-particle orbital states. Integration over dr implies the integral over τ, and the sum over all lattice states and spin projections: $\int dr \equiv \sum_i \sum_s \int_0^\beta d\tau$.

Now we switch to the interaction representation and make a perturbation series expansion for the partition function Z assuming S_0 as the unperturbed action:

$$Z = \sum_{k=0}^\infty \int dr_1 \int dr_1' \cdots \int dr_{2k} \int dr_{2k}' \Omega_k(r_1, \ldots, r_{2k}'),$$

$$\Omega_k = Z_0 \frac{(-1)^k}{k!} w_{r_1 r_2}^{r_1' r_2'} \cdots w_{r_{2k-1} r_{2k}}^{r_{2k-1}' r_{2k}'} 8 D_{r_1' r_2' \cdots r_{2k}'}^{r_1 r_2 \cdots r_{2k}},$$

$$D_{r_1' \cdots r_{2k}'}^{r_1 \cdots r_{2k}} = \langle \mathcal{T} c_{r_1'}^\dagger c^{r_1} \cdots c_{8 r_{2k}'}^\dagger c^{r_{2k}} \rangle_0. \quad \text{(B2)}$$

Here, $Z_0 = \mathrm{Tr}(\mathcal{T} e^{-S_0})$ is the partition function for the unperturbed system, the triangular brackets with the subscript

"zero" denote the average over the unperturbed system: $\langle A \rangle_0 = Z_0^{-1} \mathrm{Tr}(\mathcal{T} A e^{-S_0})$. Since S_0 is Gaussian, one can apply Wick's theorem, and therefore, $D_{r_1' \cdots r_{2k}'}^{r_1 \cdots r_{2k}}$ is the determinant of a $2k \times 2k$ matrix which consists of the bare two-point Green's functions $g_{r'}^r = \langle \mathcal{T} c_{r'}^\dagger c^r \rangle_0$:

$$D_{(2k)} \equiv D_{r_1' r_2' \cdots r_{2k}'}^{r_1 r_2 \cdots r_{2k}} = \det |g_{r_j'}^{r_i}|. \quad \text{(B3)}$$

An important property of the above formula is that the integrands remain unchanged under the permutations $r_i, r_{i'}, r_{i+1}, r_{i'+1} \leftrightarrow r_j, r_{j'}, r_{j+1}, r_{j'+1}$ with any i, j. Therefore, it is possible to introduce a quantity K, which we call "state of the system" and is a combination of the perturbation order k and an *unnumbered set* of k tetrad of coordinates. Now, denote $\Omega_K = k! \Omega_k$, where the factor $k!$ reflects all possible permutations of the arguments. In the series (B2) for the partition function, the $k!$ in the nominator and the denominator cancel each other, so that this series can be rewritten in the simple form

$$Z = \int \Omega_K D[K], \quad \text{(B4)}$$

where $\int D[K]$ means the summation over k and integration over all possible realizations of the above-mentioned unnumbered set at each k.

In a similar way, we can express the interacting two-point Green's function for the system (B1) using the perturbation series expansion (B2). It reads

$$G_{r'}^r \equiv Z^{-1} \langle \mathcal{T} c_{r'}^\dagger c^r e^{-W} \rangle_0 = Z^{-1} \int G_K \Omega_K D[K], \quad \text{(B5)}$$

where $G_K(r, r')$ is defined as

$$G_K(r, r') = \frac{\langle \mathcal{T} c_{r'}^\dagger c^r c_{r_1'}^\dagger c^{r_1} \cdots c_{r_{2k}'}^\dagger c^{r_{2k}} \rangle_0}{\langle \mathcal{T} c_{r_1'}^\dagger c^{r_1} \cdots c_{r_{2k}'}^\dagger c^{r_{2k}} \rangle_0}.$$

This is nothing else than the ratio of two determinants: $D_{(2k+1)} / D_{(2k)}$.

The important thing to notice is that the series expansion for an exponential *always* converges for finite fermionic systems. A mathematically rigorous proof can be constructed for Hamiltonian systems. Indeed, the many-body fermionic Hamiltonians H_0 and W have a finite number of eigenstates, that is, $2^{N_{orb}}$, where N_{orb} is the total number of electronic orbitals in the system. Now one can observe that $\Omega_k < \mathrm{const} \cdot W_{max}^k$, where W_{max} is the eigenvalue of W with maximal modulus. This proves the convergence of Eq. (B2) because $k!$ in the denominator grows faster than the numerator. In our calculations for non-Hamiltonian systems, we did not observe any indications of the divergence either.

Although the formulas (B4) and (B5) look rather formal, they exactly correspond to the idea of the proposed QMC scheme. We simulate a Markov random walk in the space of all possible K with a probability density $P_K \propto |\Omega_K|$ to visit each state. Two kinds of trial steps are necessary: one should try either to increase or to decrease k by 1, and, respectively, to add or to remove the corresponding tetrad of "coordi-

nates." Then the standard Metropolis acceptance criterion can be constructed using the ratio

$$\frac{\|w\|}{k+1}\left|\frac{D_{r'_1\cdots r'_{2k+2}}^{r_1\cdots r_{2k+2}}}{D_{r'_1\cdots r'_{2k}}^{r_1\cdots r_{2k}}}\right| \tag{B6}$$

for the incremental steps, and its inverse for the decremental ones. In general, one may also want to add and/or remove several tetrads simultaneously. Corresponding probabilities can be constructed in a way similar to Eq. (B6).

The most time consuming operation of the algorithm is the calculation of the ratio of determinants and Green's function matrices. It is necessary for the calculation of Monte Carlo weights as well as for the Green's functions. However, there also exist so-called fast-update formula for the calculation of the ratios of determinants and Green's function matrices. The usual procedure takes N^3 operations, while the fast-update technique requires only N^2 or less operations, where N is the matrix size. The only matrix which one needs to keep during QMC steps is the inverse matrix of the bare Green's functions: $M^{(2k)}=(g^{(2k)})^{-1}$. The fast-update formulas for the increment of the matrix size by 1 are as follows:

$$M_{i,j}^{(2k+1)}=M_{i,j}^{(2k)}-\lambda^{-1}\left(\sum_{i'}M_{i,i'}^{(2k)}g_{i'}^{2k+1}\right)\left(\sum_{j'}g_{2k+1}^{j'}M_{j'j}^{(2k)}\right),$$

$$\lambda=1+\sum_{i'j'}g_{2k+1}^{j'}M_{j'i'}^{(2k)}g_{i'}^{2k+1}, \tag{B7}$$

as can be checked by matrix multiplication of Eq. (B7) with $g^{(2k+1)}$. Here, the indices take the values $1,\ldots,2k+1$, and the matrix $M_{(2k)}$ is enlarged to a $(2k+1)\times(2k+1)$ matrix with $M_{2k+1,2k+1}=1$ and $M_{2k+1,i}=0$, $M_{i,2k+1}=0$. The factor λ appears to be exactly the ratio of the determinants. An incremental step $k\rightarrow k+1$ consists of the two updates (B7). One can see that the formula, indeed, have an N^2 complexity.

A decrement of the matrix size is similar:

$$M_{i,j}^{(2k-1)}=M_{i,j}^{(2k)}-\lambda^{-1}\left(\sum_{i'}M_{i,i'}^{(2k)}g_{i'}^{2k}\right)\left(\sum_{j'}g_{2k}^{j'}M_{j'j}^{(2k)}\right),$$

$$\lambda=1+\sum_{i'j'}g_{2k}^{j'}M_{j'i'}^{(2k)}g_{i'}^{2k}. \tag{B8}$$

It can be shown that for the decrement step, λ, in fact, equals the simple ratio $M_{2k2k}^{(2k)}/g_{2k}^{2k}$.

With the matrix M, the Green's function can be obtained both in imaginary time and at Matsubara frequencies:

$$G_{\tau'}^{\tau}=g_{\tau'}^{\tau}-\sum_{i,j}g_{\tau_i}^{\tau}M_{i,j}g_{\tau'}^{\tau_j},$$

$$G(\omega)=g(\omega)-g(\omega)\left[\frac{1}{\beta}\sum_{i,j}M_{i,j}e^{i\omega(\tau_i-\tau_j)}\right]g(\omega). \tag{B9}$$

Here, $g_{\tau'}^{\tau}$ and $g(\omega)$ are the bare Green's function in imaginary time and Matsubara spaces, respectively.

In order to reduce and, in some cases, avoid the sign problem in CT-QMC, we introduce additional quantities $\alpha_{r'}^{r}$,

which, in principle, can be functions of time, spin, and the number of lattice states. Thus, up to an additive constant, we have the new separation of our action:

$$S_0=\int\int\left[t_r^{r'}+\int\int\alpha_{r_2}^{r_2}(w_{rr_2}^{r'r'_2}+w_{r_2r}^{r'_2r'})dr_2dr'_2\right]c_{r'}^\dagger c^r drdr',$$

$$W=\int\int\int\int w_{r_1r_2}^{r'_1r'_2}(c_{r'_1}^\dagger c^{r_1}-\alpha_{r'_1}^{r_1})(c_{r'_2}^\dagger c^{r_2}-\alpha_{r'_2}^{r_2})dr_1dr'_1dr_2dr'_2.$$

In this case, the determinants $D_{r'_1\cdots r'_{2k}}^{r_1\cdots r_{2k}}$ of $2k\times 2k$ matrices have the following form:

$$D_{r'_1r'_2\cdots r'_{2k}}^{r_1r_2\cdots r_{2k}}=\det|g_{r'_j}^{r_i}-\alpha_{r'_j}^{r_i}\delta_{ij}|, \tag{B10}$$

where $i,j=1,\ldots,2k$. A proper choice of α can completely remove the sign problem. For example, in the case of the Hubbard model, the choice $\alpha_\uparrow=1-\alpha_\downarrow$ eliminates the sign problem for repulsive systems with particle-hole symmetry. Note, however, that the proper choice of the α's depends on the particular system under consideration. For the calculation presented in this paper, we use the symmetrized expression for the interaction:

$$W=\frac{1}{2}\sum_{mm'\sigma\sigma'}(U_{mm'}-\delta_{\sigma\sigma'}J_{mm'})(n_m^\sigma-\alpha)(n_{m'}^{\sigma'}-1+\alpha). \tag{B11}$$

With this form of interaction, a small negative α was found to eliminate the sign problem completely. The value of $\alpha=-0.01$ was used in the calculation.

Let us now describe how the global updates can be implemented in CT-QMC calculation for the insulating phase. This trick is useful in getting rid of the local trapping of the Markov random walk for the system with reasonably small orbital or spin polarization, especially for insulating systems. Another possibility to eliminate local trapping would be to use quantum Wang-Landau procedure.[57] Although it is also implemented in CT-QMC code, we realized that global updates are practically much more efficient for our case.

To analyze the structure of perturbation series (B5), it is useful to consider an atomic limit $\mathcal{G}^{-1}=i\omega+\mu$. In this case, the last line of Eq. (B2) is composed of particle-number operators which actually do not depend on time argument, because $n_{s\sigma}$ commutes with the noninteracting part of the action. Therefore, the average (B10) can be calculated according to the formula $\langle(n_1^\uparrow-\alpha)^{k_1}(n_1^\uparrow-1+\alpha)^{k'_1}\cdots(n_3^\downarrow-\alpha)^{k_6}(n_3^\downarrow-1+\alpha)^{k'_6}\rangle_0$ with certain power indices $k_1,k'_1,\ldots,k_6,k'_6$. Since for Fermi operators $n=n^2$, it can be easily shown that $(n_m^\sigma-\alpha)^k(n_m^\sigma-1+\alpha)^{k'}=(-\alpha)^k(\alpha-1)^{k'}(1-n_m^\sigma)+(1-\alpha)^k\alpha^{k'}n_m^\sigma$. Coefficients here fall down exponentially as k and k' grow. Therefore, qualitatively speaking, the expression is remarkably large if either k or k' equals zero. We conclude that the partition function is at most contributed by such terms that 6 of 12 power indices vanish. The other six indices are large; their typical value in calculation is $k\propto\beta U\gg 1$ (Ref. 35). In an elementary CT-QMC move,[58] the value of k is changed to $k+1$ or $k-1$. Clearly, it is hard to

switch, for example, from the situation $k_1 \geqslant 1, k_1' = 0$ to $k_1 = 0, k_1' \geqslant 1$, and therefore, the program becomes trapped in a configuration with a certain set of vanished indices. It can be shown that an exponential barrier separates the traps. Practically, this results in an incorrect calculation output with non-physically large spin and/or orbital polarization.

DMFT calculation for test systems convinced us that the trapping remains important also far from atomic limit, until the system is in the insulating state. For metallic phase, the barriers disappear.

To get rid of trapping, we introduce a special kind of Monte Carlo steps, so called global updates for orbital and spin indices. During global update, the program permutes randomly orbital and spin indices of the current realization: $m \rightarrow \tilde{m}, \sigma \rightarrow \tilde{\sigma}$. After this, the weight of the new configuration should be calculated. This requires the calculation of the factor

$$\langle [n_{\tilde{m}_1}^{\tilde{\sigma}_1}(\tau_1) - \alpha][n_{\tilde{m}_1'}^{\tilde{\sigma}_1'}(\tau_1) - 1 + \alpha] \cdots [n_{\tilde{m}_k}^{\tilde{\sigma}_k}(\tau_k) - \alpha][n_{\tilde{s}_k'}^{\tilde{\sigma}_k'}(\tau_k) - 1$$

$+ \alpha]\rangle_0$. All other quantities affecting the weight of the configuration remain the same, because the interaction part is symmetrical with respect to permutations of spin and orbital indices. Moves are accepted according to a standard Metropolis criterion. Without orbital splitting, all local minima are equivalent, therefore, a global update actually does not change the weight factor, and the move is always accepted. For a small orbital field, the acceptance rate of the global moves remains high enough.

During the global update, averages over the Gaussian part of the action should be calculated from scratch. Therefore, a global update requires $\propto k^3$ operations. The operation count for elementary CT-QMC move is $\propto k^2$ because of the fast-update trick. Therefore, we perform global updates much more rarely than the elementary CT-QMC move. This turns out to be sufficient to get rid of the local trapping.

[1] For a review, see N. F. Mott, *Metal-Insulator Transitions* (Taylor and Francis, London, 1990). W. Brückner, H. Oppermann, W. Reichelt, J. I. Terukow, F. A. Tschudnowski, and E. Wolf, *Vanadiumoxide Darstellung, Eigenschaften, Anwendung* (Akademie, Berlin, 1983).

[2] D. B. McWhan and T. M. Rice, Phys. Rev. Lett. **22**, 887 (1969); D. B. McWhan, T. M. Rice, and J. P. Remeika, *ibid.* **23**, 1384 (1969).

[3] H. Kuwamoto, J. M. Honig, and J. Appel, Phys. Rev. B **22**, 2626 (1980).

[4] G. A. Thomas, D. H. Rapkine, S. A. Carter, A. J. Millis, T. F. Rosenbaum, P. Metcalf, and J. M. Honig, Phys. Rev. Lett. **73**, 1529 (1994).

[5] S. Shin, S. Suga, M. Taniguchi, M. Fujisawa, H. Kanzaki, A. Fujimori, H. Daimon, Y. Ueda, K. Kosuge, and S. Kachi, Phys. Rev. B **41**, 4993 (1990); S. Shin, Y. Tezuka, T. Kinoshita, T. Ishii, T. Kashiwakura, M. Takahashi, and Y. Suda, J. Phys. Soc. Jpn. **64**, 1230 (1995).

[6] G. A. Sawatzky and D. Post, Phys. Rev. B **20**, 1546 (1979).

[7] M. Schramme, Ph.D. thesis, Universität Augsburg, 2000; E. Goering, M. Schramme, O. Müller, H. Paulin, M. Klemm, M. L. denBoer, and S. Horn, Physica B **230-232**, 996 (1997).

[8] S.-K. Mo, J. D. Denlinger, H.-D. Kim, J.-H. Park, J. W. Allen, A. Sekiyama, A. Yamasaki, K. Kadono, S. Suga, Y. Saitoh, T. Muro, P. Metcalf, G. Keller, K. Held, V. Eyert, V. I. Anisimov, and D. Vollhardt, Phys. Rev. Lett. **90**, 186403 (2003).

[9] S.-K. Mo *et al.*, Phys. Rev. Lett. **93**, 076404 (2004).

[10] D. B. McWhan, J. P. Remeika, T. M. Rice, W. F. Brinkman, J. P. Maita, and A. Menth, Phys. Rev. Lett. **27**, 941 (1971).

[11] C. Castellani, C. R. Natoli, and J. Ranninger, Phys. Rev. B **18**, 4945 (1978); **18**, 5001 (1978).

[12] M. J. Rozenberg, G. Kotliar, H. Kajueter, G. A. Thomas, D. H. Rapkine, J. M. Honig, and P. Metcalf, Phys. Rev. Lett. **75**, 105 (1995).

[13] J.-H. Park, L. H. Tjeng, A. Tanaka, J. W. Allen, C. T. Chen, P. Metcalf, J. M. Honig, F. M. F. deGroot, and G. A. Sawatzky, Phys. Rev. B **61**, 11506 (2000).

[14] F. Mila, R. Shiina, F. C. Zhang, A. Joshi, M. Ma, V. I. Anisimov, and T. M. Rice, Phys. Rev. Lett. **85**, 1714 (2000).

[15] S. DiMatteo, N. B. Perkins, and C. R. Natoli, Phys. Rev. B **65**, 054413 (2002).

[16] L. F. Mattheiss, J. Phys.: Condens. Matter **6**, 6477 (1994).

[17] S. Y. Ezhov, V. I. Anisimov, D. I. Khomskii, and G. A. Sawatzky, Phys. Rev. Lett. **83**, 4136 (1999).

[18] I. S. Elfimov, T. Saha-Dasgupta, and M. A. Korotin, Phys. Rev. B **68**, 113105 (2003).

[19] V. Eyert, U. Schwingenschlögl, and U. Eckern, Europhys. Lett. **70**, 782 (2005).

[20] K. Held, G. Keller, V. Eyert, D. Vollhardt, and V. I. Anisimov, Phys. Rev. Lett. **86**, 5345 (2001).

[21] G. Keller, K. Held, V. Eyert, D. Vollhardt, and V. I. Anisimov, Phys. Rev. B **70**, 205116 (2004); D. Vollhardt *et al.*, J. Phys. Soc. Jpn. **74**, 136 (2005).

[22] U. K. Poulsen, J. Kollar, and O. K. Andersen, J. Phys. F: Met. Phys. **6**, L241 (1976).

[23] G. Sawatzky, recorded talk at the Kavli Institute for Theoretical Physics, UCSB, 2002.

[24] V. I. Anisimov, D. E. Kondakov, A. V. Kozhevnikov, I. A. Nekrasov, Z. V. Pchelkina, J. W. Allen, S.-K. Mo, H.-D. Kim, P. Metcalf, S. Suga, A. Sekiyama, G. Keller, I. Leonov, X. Ren, and D. Vollhardt, Phys. Rev. B **71**, 125119 (2005). In order to avoid the fixed hybridization approximation, one needs to carry out the full **k** sum in the self-consistency condition [Eq. (8)]. This can either be done by using the full set of nearly orthonormal LMTOs corresponding to the valence orbitals, as has been done in transition metals (Refs. 25 and 46) but is technically involved for transition metal oxides (due the strong hybridization), or the set must be downfolded to t_{2g} Wannier functions. The above-mentioned paper presents a way of doing this. The first consistent use of the Wannier representation in LDA+DMFT calculations was by Pavarini *et al* (Ref. 29).

[25] M. I. Katsnelson and A. I. Lichtenstein, J. Phys.: Condens. Matter **11**, 1037 (1999); A. I. Lichtenstein, M. I. Katsnelson, and G. Kotliar, Phys. Rev. Lett. **87**, 067205 (2001).

[26] M. S. Laad, L. Craco, and E. Müller-Hartmann, Phys. Rev. B **73**, 045109 (2006); Phys. Rev. Lett. **91**, 156402 (2003).

[27] T. Saha-Dasgupta, J. Nuss, O. K. Andersen, A. I. Lichtenstein, A. I. Poteryaev, and A. Georges (unpublished).

[28] O. K. Andersen and T. Saha-Dasgupta, Phys. Rev. B **62**, R16219 (2000), and references therein.

[29] E. Pavarini, S. Biermann, A. I. Poteryaev, A. I. Lichtenstein, A. Georges, and O. K. Andersen, Phys. Rev. Lett. **92**, 176403 (2004); E. Pavarini, A. Yamasaki, J. Nuss, and O. K. Andersen, New J. Phys. **7**, 188 (2005).

[30] N. Marzari and D. Vanderbilt, Phys. Rev. B **56**, 12847 (1997).

[31] F. Lechermann, A. Georges, A. Poteryaev, S. Biermann, M. Posternak, A. Yamasaki, and O. K. Andersen, Phys. Rev. B **74**, 125120 (2006).

[32] R. Frésard and G. Kotliar, Phys. Rev. B **56**, 12909 (1997).

[33] I. Solovyev, N. Hamada, and K. Terakura, Phys. Rev. B **53**, 7158 (1996).

[34] J. E. Hirsch and R. M. Fye, Phys. Rev. Lett. **56**, 2521 (1986).

[35] A. N. Rubtsov, arXiv:cond-mat/0302228 (unpublished); A. N. Rubtsov and A. I. Lichtenstein, JETP Lett. **80**, 61 (2004); A. N. Rubtsov, V. V. Savkin, and A. I. Lichtenstein, Phys. Rev. B **72**, 035122 (2005).

[36] A. Georges and G. Kotliar, Phys. Rev. B **45**, 6479 (1992); H. Kajueter and G. Kotliar, Phys. Rev. Lett. **77**, 131 (1996).

[37] T. Pruschke and N. Grewe, Z. Phys. B: Condens. Matter **74**, 439 (1989); M. Jarrell and T. Pruschke, *ibid.* **90**, 187 (1993); Phys. Rev. B **49**, 1458 (1994).

[38] S. Savrasov, G. Kotliar, and E. Abrahams, Nature (London) **410**, 293 (2001); L. Chioncel, L. Vitos, I. A. Abrikosov, J. Kollár, M. I. Katsnelson, and A. I. Lichtenstein, Phys. Rev. B **67**, 235106 (2003); J. Minár, L. Chioncel, A. Perlov, H. Ebert, M. I. Katsnelson, and A. I. Lichtenstein, *ibid.* **72**, 045125 (2005).

[39] M. Jarrell and J. E. Gubernatis, Phys. Rep. **269**, 133 (1996).

[40] J. M. Tomczak and S. Biermann, J. Phys. Condens Mattter (to be published); J. M. Tomczak, F. Aryasetiawan, and S. Biermann, arXiv:0704.0902 (unpublished).

[41] Spectral functions along other directions available upon request from jan.tomczak@polytechnique.edu

[42] M. Jarrell, J. K. Freericks, and Th. Pruschke, Phys. Rev. B **51**, 11704 (1995).

[43] N. Blümer, Ph.D. thesis, Universität Augsburg, 2002.

[44] I. A. Nekrasov, K. Held, G. Keller, D. E. Kondakov, T. Pruschke, M. Kollar, O. K. Andersen, V. I. Anisimov, and D. Vollhardt, Phys. Rev. B **73**, 155112 (2006).

[45] A. I. Lichtenstein and M. I. Katsnelson, Phys. Rev. B **57**, 6884 (1998).

[46] S. Biermann, A. Dallmeyer, C. Carbone, W. Eberhardt, C. Pampuch, O. Rader, M. I. Katsnelson, and A. I. Lichtenstein, JETP Lett. **80**, 612 (2004); arXiv:cond-mat/0112430 (unpublished).

[47] We perform the fit below the coherence temperature where we can use the zero temperature form of the self-energy.

[48] It is easy to see that the construction using the unhybridized band structure is better than using the full LDA band structure as long as the crystal-field splitting of the former (that is, the difference of the local LDA levels) is smaller than the hybridization. In that case, the construction using the unhybridized bands coincides with the real quasiparticle band structure up to second order in the hybridization, whereas the usage of the LDA induces a first-order error.

[49] I. Turek, V. Drchal, J. Kudrnovsky, M. Sob, and P. Weinberger, *Electronic Structure of Disordered Alloys, Surfaces and Interfaces* (Kluwer Academic, Boston, 1997).

[50] T. Saha-Dasgupta, A. Lichtenstein, and R. Valenti, Phys. Rev. B **71**, 153108 (2005).

[51] We note that, strictly speaking, it is *not enough* that the crystal-field splitting exceeds the value of $\max \epsilon_{e_g^\pi} - \min \epsilon_{a_{1g}}$, but one has to have separately $\min \epsilon_{a_{1g}} + \Re\Sigma_{a_{1g}}(0) > 0$ and $\max \epsilon_{e_g^\pi} + \Re\Sigma_{e_g^\pi}(0) < 0$; that is, one has to push the top of the e_g^π band below and the bottom of the a_{1g} band above the Fermi level. This is only roughly the same condition, since due to the largely incoherent character of the e_g^π bands, Luttinger's theorem does not hold.

[52] A. Yamasaki, M. Feldbacher, Y. F. Yang, O. K. Andersen, and K. Held, Phys. Rev. Lett. **96**, 166401 (2006).

[53] A. Sekiyama *et al.*, Phys. Rev. Lett. **93**, 156402 (2004).

[54] J. E. Hirsch, Phys. Rev. B **28**, 4059 (1983).

[55] A. I. Poteryaev, A. I. Lichtenstein, and G. Kotliar, Phys. Rev. Lett. **93**, 086401 (2004).

[56] S. Biermann, A. I. Poteryaev, A. I. Lichtenstein, and A. Georges, Phys. Rev. Lett. **94**, 026404 (2005).

[57] M. Troyer, S. Wessel, and F. Alet, Phys. Rev. Lett. **90**, 120201 (2003).

[58] A. Georges, G. Kotliar, W. Krauth, and M. Rozenberg, Rev. Mod. Phys. **68**, 13 (1996).